# Continuous GPS measurements of postglacial adjustment in Fennoscandia:
# 2. Modeling results

Glenn A. Milne,[1] Jerry X. Mitrovica,[2] Hans-Georg Scherneck,[3] James L. Davis,[4] Jan M. Johansson,[3] Hannu Koivula,[5] and Martin Vermeer[6]

[1]  Data collected under the auspices of the BIFROST GPS project yield a geographically dense suite of estimates of present-day, three-dimensional (3-D) crustal deformation rates in Fennoscandia [*Johansson et al.*, 2002]. A preliminary forward analysis of these estimates [*Milne et al.*, 2001] has indicated that models of ongoing glacial isostatic adjustment (GIA) in response to the final deglaciation event of the current ice age are able to provide an excellent fit to the observed 3-D velocity field. In this study we revisit our previous GIA analysis by considering a more extensive suite of forward calculations and by performing the first formal joint inversion of the BIFROST rate estimates. To establish insight into the physics of the GIA response in the region, we begin by decomposing a forward prediction into the three contributions associated with the ice, ocean, and rotational forcings. From this analysis we demonstrate that recent advances in postglacial sea level theory, in particular the inclusion of rotational effects and improvements in the treatment of the ocean load in the vicinity of an evolving continental margin, involve peak signals that are larger than the observational uncertainties in the BIFROST network. The forward analysis is completed by presenting predictions for a pair of Fennoscandian ice histories and an extensive suite of viscoelastic Earth models. The former indicates that the BIFROST data set provides a powerful discriminant of such histories. The latter yields bounds on the (assumed constant) upper and lower mantle viscosity ($\nu_{UM}$, $\nu_{LM}$); specifically, we derive a 95% confidence interval of $5 \times 10^{20} \leq \nu_{UM} \leq 10^{21}$ Pa s and $5 \times 10^{21} \leq \nu_{LM} \leq 5 \times 10^{22}$ Pa s, with some preference for (elastic) lithospheric thickness in excess of 100 km. The main goal of the (Bayesian) inverse analysis is to estimate the radial resolving power of the BIFROST GPS data as a function of depth in the mantle. Assuming a reasonably accurate ice history, we demonstrate that this resolving power varies from ∼200 km near the base of the upper mantle to ∼700 km in the top portion of the lower mantle. We conclude that the BIFROST data are able to resolve structure on radial length scale significantly smaller than a single upper mantle layer. However, these data provide little constraint on viscosity in the bottom half of the mantle. Finally, elements of both the forward and inverse analyses indicate that radial and horizontal velocity estimates provide distinct constraints on mantle viscosity.
*INDEX TERMS:* 1208 Geodesy and Gravity: Crustal movements—intraplate (8110); 1236 Geodesy and Gravity: Rheology of the lithosphere and mantle (8160); 8107 Tectonophysics: Continental neotectonics; *KEYWORDS:* glacial isostasy, space geodesy, mantle viscosity

[1]Department of Earth Sciences, University of Durham, Durham, UK.
[2]Department of Physics, University of Toronto, Toronto, Ontario, Canada.
[3]Onsala Space Observatory, Chalmers University of Technology, Onsala, Sweden.
[4]Harvard-Smithsonian Center for Astrophysics, Cambridge, Massachusetts, USA.
[5]Finnish Geodetic Institute, Masala, Finland.
[6]Institute of Geodesy, Helsinki University of Technology, Espoo, Finland.

## 1.  Introduction

[2]  Baseline Inferences for Fennoscandian Rebound Observations Sea Level and Tectonics (BIFROST) [*BIFROST Project*, 1996] is a project initiated in 1993 to directly measure the present-day, three-dimensional (3-D) crustal deformation in Fennoscandia. A dense array of continuously operating GPS (Global Positioning System) receivers was deployed between 1993 and 1997 to achieve this objective. The BIFROST GPS network is composed of two subnetworks, the Swedish SWEPOS™ network
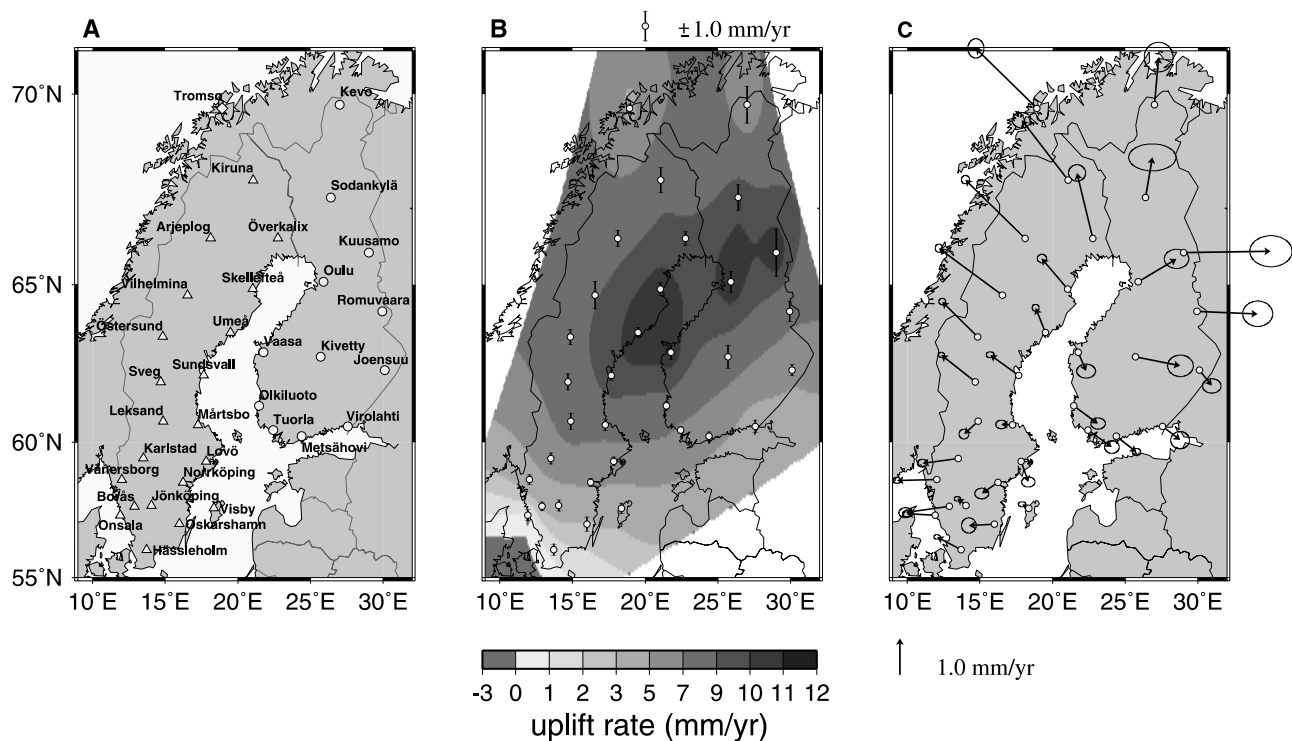
**Figure 1.** (a) Map showing the locations of 34 GPS receiver sites in the BIFROST GPS network. The network comprises 21 SWEPOS™ stations (triangles) and 12 FinnRef™ stations (circles). Data from the IGS (International GPS Service) site Tromsø (diamond) are also employed in the analysis. Note that the sites are distributed uniformly over most of Sweden and Finland. (b) Contour map of the present-day vertical velocity field. The locations of the GPS sites are shown by grey circles and the site-specific 1σ uncertainty is superimposed at each location (error scale at top). (c) The present-day horizontal velocity determined for each site. The 1σ error ellipses are shown (scale vector at bottom). Site locations are marked by grey circles. The observational errors shown are scaled values of the formal uncertainties determined for each site. The scaling factor is computed as part of the GPS data processing analysis to quantify the contribution of a number of potential error sources (see paper 1). It is important to note that the errors shown in Figures 1b and 1c are estimates of the true uncertainty [see, e.g., *Mäkinen et al.*, 2003; *Scherneck et al.*, 2003].

(21 receivers) and the Finnish FinnRef™ network (12 receivers) which, together, provide a relatively uniform and complete spatial sampling of crustal motion in Sweden and Finland (see Figure 1a for site locations).

[3] The companion paper by *Johansson et al.* [2002] (hereinafter referred to as paper 1) focused on data analysis procedures adopted to obtain the geodetic estimates of crustal deformation and on the primary sources of error associated with the GPS data analysis. The site velocities resulting from the BIFROST standard solution (see paper 1) are plotted in Figures 1b and 1c. The vertical rates (Figure 1b) map into a broad, ellipsoidal region of uplift with an axis of symmetry lying approximately southwest to northeast. The maximum, site-specific, rate of 11.2 mm/yr is recorded at Umeå. The horizontal deformation field is characterized by motions directed outward from the zone of maximum crustal uplift. The amplitude of these horizontal motions exceeds 2 mm/yr at several sites (e.g., Tromsø, Arjeplog).

[4] The 3-D crustal velocities estimated from the BIFROST network exhibit geometries that are consistent with numerical models of glacial isostatic adjustment (GIA) [e.g., *James and Lambert*, 1993; *Mitrovica et al.*, 1994b]. A preliminary modeling analysis in paper 1 showed that pre-

dictions based on a single ice-Earth model pair tuned to fit a regional sea level database yields a good fit to the BIFROST results, suggesting that GIA is the dominant contribution to the observed signal. This was confirmed by *Milne et al.* [2001], who provided an overview of the application of BIFROST constraints to the problems of inferring mantle viscosity, estimating ongoing regional sea level rise and bounding neotectonic motions in Fennoscandia.

[5] Models of the GIA process in Fennoscandia have traditionally been constrained using relative sea level observations obtained from sea level markers within the geological record or from the regional tide gauge network. These sea level data have been used in a large number of analyses to infer GIA model parameters relating to subsurface viscosity structure [e.g., *Haskell*, 1935; *Veining Meinesz*, 1937; *McConnell*, 1968; *Wolf*, 1987; *Fjeldskaar*, 1994; *Mitrovica*, 1996; *Lambeck et al.*, 1998a; *Davis et al.*, 1999; *Wieczerkowski et al.*, 1999] and the deglaciation history of the most recent Fennoscandian ice sheet [e.g., *Tushingham and Peltier*, 1991; *Lambeck et al.*, 1998a]. Unfortunately, while the Fennoscandian database of sea level observations is relatively large, it remains insufficient to uniquely constrain either the loading history or the Earth

model for the region or, in fact, to completely separate the sensitivities of the observations to these two fundamental inputs to the GIA problem.

[6] These obstacles are common to all GIA analyses, and efforts to overcome them involve one of two approaches. First, one can seek parameterizations of the data that exhibit a reduced sensitivity to the uncertain ice history [e.g., *McConnell*, 1968; *Nakada and Lambeck*, 1989; *Mitrovica and Peltier*, 1993]. Second, one can introduce new data types with complementary sensitivities. In regards to GIA analysis within Fennoscandia, the BIFROST data sets provide a novel route toward the latter. For example, a key limitation of sea level data, both geological and tide gauge, is their relatively poor spatial distribution [see, e.g., *Lambeck et al.*, 1998a, Figure 20]; in particular, these data are confined to coastal regions and so provide a relatively sparse sampling of the region of uplift. The BIFROST data, in contrast, provide an improved spatial coverage that more uniformly samples the Fennoscandian deformation field. In addition, while sea level data constrain only the vertical component of GIA, the GPS network yields estimates of the full 3-D deformation field. The horizontal component of GIA-induced deformation has been shown to have sensitivities to variations in the Earth model and ice history that are distinct from those of the vertical component [*Mitrovica et al.*, 1994a, 1994b].

[7] The present study is motivated by the unique constraints on GIA models provided by the BIFROST network, and our goal is to revisit, in detail, the "excellent fit" to the GPS data described in previous numerical GIA studies. We begin by decomposing forward analyses of the present-day Fennoscandian deformation field into contributions associated, for example, with ice and ocean loading, rotational effects, etc., in order to clarify the physics of the GIA response in this region. We next explore the potential of the BIFROST data to constrain models of the GIA process by considering predictions based on forward analyses of the BIFROST data involving two regional ice models and a large sequence of Earth models distinguished on the basis of the thickness of the (elastic) lithosphere and the (assumed constant) viscosity within either the upper or lower mantle. Forward analyses are a relatively crude method for exploring constraints on Earth structure provided by the GPS estimates of 3-D crustal velocity. Accordingly, we complete the paper by providing the first multilayer formal inversion of the BIFROST data. The primary goal of the inversion is to generate estimates of the detailed, depth-dependent resolving power of the GPS data.

## 2. Forward Model

[8] In general, numerical models of the GIA process require two inputs: A representation of the GIA forcing and a rheological model of the solid Earth that governs the response to the forcing. Following the vast majority of previous GIA studies, we adopt a Maxwell viscoelastic rheology in our modeling. The extent to which a simple linear rheology of the Maxwell type is valid for the Earth's mantle on GIA timescales remains a matter of ongoing discussion [e.g., *Karato and Wu*, 1993; *Wu*, 1999]. However, there is also broad consensus that the Maxwell viscoelastic rheology has proven to be the simplest model

that can provide acceptable fits to a variety of GIA data types.

[9] The Earth models we adopt are spherically symmetric (i.e., physical properties are invariant with longitude and latitude), and self-gravitating. The models are compressible in the elastic limit and incompressible in the (long time-scale) fluid limit (see *Wu and Peltier* [1982] for complete details). The elastic and density structure, which is the same for each model, of the models has a depth discretization of 25 km throughout the mantle and is taken from the seismic model PREM [*Dziewonski and Anderson*, 1981]. The radial profile of viscosity, which is more crudely depth parameterized into three layers, is a free parameter of the modeling (see section 3).

[10] Computing the response of such an Earth model to a forcing that includes a surface (ice plus ocean) mass load and perturbations in the rotational state is a relatively complex undertaking [e.g., see *Peltier*, 1974; *Mitrovica et al.*, 1994a; *Milne et al.*, 1999; *Mitrovica et al.*, 2001]. The main elements of the mathematical formalism are briefly described in Appendix A. In the following, we outline the general steps in the calculation, paying particular attention to new developments that are relevant to results described in section 3.

[11] Our calculation of present-day 3-D crustal motions proceeds as follows. First, with the viscoelastic Earth model specified, we compute all the parameters defining the Love numbers (equations (A1) to (A4)), using the approach specified by *Peltier* [1974] and *Wu* [1978]. Second, for a given model of the late Pleistocene ice history we solve the sea level equation recently derived by *Milne* [1998] and *Milne et al.* [1999]. The new sea level theory incorporates a series of improvements to the traditional approach described by *Farrell and Clark* [1976], including a revised treatment of the sea level response in the vicinity of an evolving ocean-continent margin and the incorporation of consistent GIA-induced perturbations to the model Earth's rotation vector. This sea level equation provides, on output, the spherical harmonic decomposition of the ocean load, and thus at this stage the total surface mass load as a function of time, $L_{\ell,m}(t)$ in equations (A8) and (A9), is completely specified. A second output of the theory is a time-dependent perturbation in the rotation vector.

[12] Perturbations to the rotation vector are computed within the sea level theory by solving a linearized version of the Euler equation [e.g., *Sabadini et al.*, 1982; *Wu and Peltier*, 1984; *Mitrovica and Milne*, 1998; *Mitrovica et al.*, 2001]. Expressions required to map these perturbations into spherical harmonic coefficients of the change in the rotational potential, $\Lambda_{\ell,m}(t)$ in equations (A8) and (A9), are given by Mitrovica and *Milne* [1998] and *Mitrovica et al.* [2001]. To produce accurate predictions of the present rate of change of the rotation vector, and the associated rotational potential, this aspect of the computation is performed over seven full glacial cycles [e.g., *Sabadini and Vermeersen*, 1997]. The resulting time series, $\Lambda_{\ell,m}(t)$, provides the final component of the GIA-forcing required in our expressions (A8) and (A9) that give the spherical harmonic coefficients of the 3-D crustal displacement response.

[13] The computation of 3-D crustal motions is, at this stage, straightforward. The Love number parameters (equations (A1)–(A4)) are used to establish the impulse response

of the Earth model and these, together with the spherical harmonic coefficients of the surface mass load, $L_{\ell,m}$, and rotational potential, $\Lambda_{\ell,m}$, are applied to equations (A8) and (A9). Solving these equations yields, following equations (A5) and (A6), the coefficients in the spectral decompositions of the vertical and horizontal components of the crustal motion, respectively.

## 3. Modeling Results

### 3.1. Forward Analysis

[14] In previous work we were concerned solely with the ability of the numerical predictions to fit the BIFROST estimates of 3-D deformation in Fennoscandia. To begin this section we decompose a specific prediction that provides a good fit to these data into the contributions associated with each of the three GIA forcings (ice load, ocean load, and rotational potential). The three-layer radial viscosity model includes a top layer of thickness 96 km in which the viscosity is set to very large values in order to simulate an elastic lithosphere. The viscosity in the upper mantle, extending from the base of the lithosphere to the 670 km seismic discontinuity, is $5 \times 10^{20}$ Pa s, and the viscosity within the lower mantle, the region from 670 km to the top of the core, is set to $5 \times 10^{21}$ Pa s. This viscosity model provides a good fit to the BIFROST data [e.g., *Milne et al.*, 2001]; it is also compatible with a number of recent inferences, based on various parameterizations of Fennoscandian sea level data, which are relatively insensitive to details of the ice sheet history [*Mitrovica*, 1996; *Wieczerkowski et al.*, 1999].

[15] In regard to a global ice model, we adopt the ICE-3G history of *Tushingham and Peltier* [1991] but replace the Fennoscandian and Barents Sea component of this history with the regional model proposed by *Lambeck et al.* [1998a] (hereafter referred to as the LSJ model). The latter has been shown to provide a good fit to the Fennoscandian database of relative sea level histories [*Lambeck et al.*, 1998a, 1998b]. The complementary ocean load is computed by solving several versions of the so-called sea level equation (see below); in all cases, the sea level response is computed by employing the pseudospectral technique [*Mitrovica and Peltier*, 1991; *Milne et al.*, 1999] with a spherical harmonic truncation at degree and order 256.

[16] Figure 2 shows a series of predictions of radial crustal velocity. Figure 2a shows the total response generated using the ice history and Earth model specified above, together with an ocean load computed using the nonrotating form of the new sea level formalism derived by *Milne* [1998] and *Milne et al.* [1999]. In Figures 2b and 2c this signal is decomposed into the ice and ocean load signals, respectively. The total signal (Figure 2a) peaks at $10-11$ mm/yr near the sites Skellefteå and Umeå. It is clear that the ice loading dominates the magnitude and geometry of the present-day radial deformation response. The local ocean load, in comparison, contributes $10-20\%$ of the total signal with peak amplitudes that are localized, not surprisingly, in the Gulf of Bothnia. The magnitude of the ocean-load-induced signal varies from 0.05 to 1.2 mm/yr at the GPS receiver locations. Given that the uncertainties in the vertical rates are generally submillimeters per year (see Figure 1 and paper 1) and that these errors will continue to improve as the GPS time series
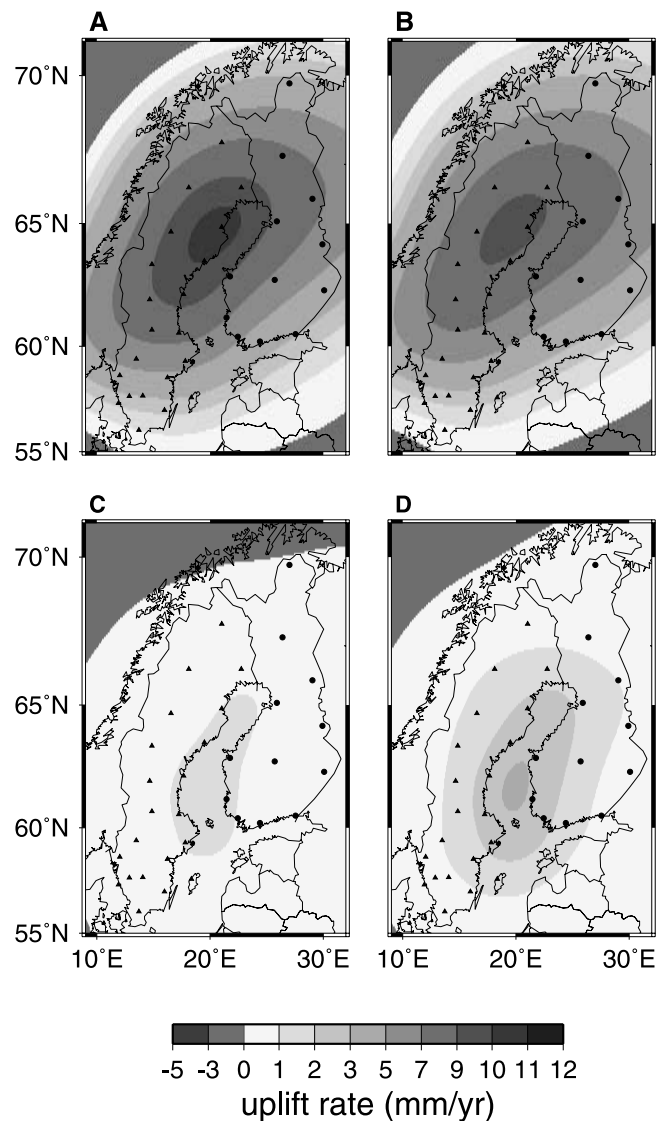


**Figure 2.** Forward predictions of the radial component of present-day crustal velocity due to different components of the GIA surface loading: (a) both ice and ocean components; (b) ice component only; (c) ocean component only; and (d) ocean component predicted by solving the original sea level equation of *Farrell and Clark* [1976]. GPS receiver locations are indicated in accordance with Figure 1a.

are extended, the signal from the ocean load, though relatively small, is certainly significant.

[17] The sea level theory described by *Milne* [1998] incorporates, among other things, a significant improvement in the treatment of the water load in the vicinity of regions vacated by ablating ice relative to the original equation derived by *Farrell and Clark* [1976]. This improvement is illustrated in Figure 3 for the period in which ice retreats from the Gulf of Bothnia.

[18] Figure 3 (left) shows the ice thickness in three snapshots from 11.6 to 8.8 ka, during which time the Fennoscandian region becomes ice free. Figure 3 (middle) shows the variation in the ocean load predicted using the new sea level theory of *Milne* [1998]. As an example,
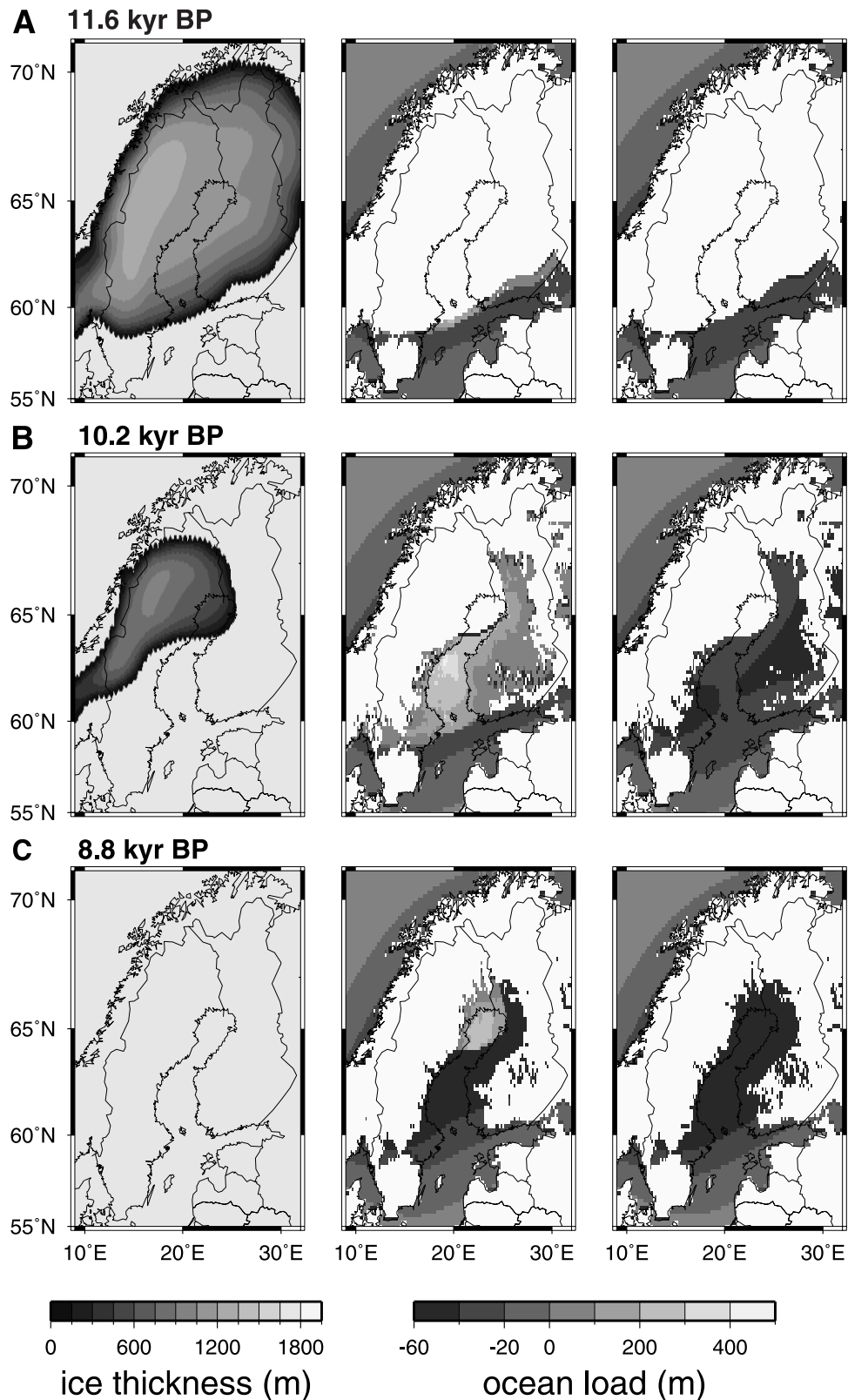
**Figure 3.** Components of the regional surface load during the last stages of deglaciation. (left) Ice thickness at the times (a) 11.6, (b) 10.2, and (c) 8.8 ka. These times correspond to the calibrated ^{14}C timescale. (middle and right) Predicted ocean load at the corresponding time steps predicted via the revised [*Milne et al.*, 1999] and original [*Farrell and Clark*, 1976] sea level equations, respectively. In Figure 3 (middle and right) the areas with light grey shading denote regions that are either ice covered or above contemporaneous sea level. See color version of this figure at back of this issue.
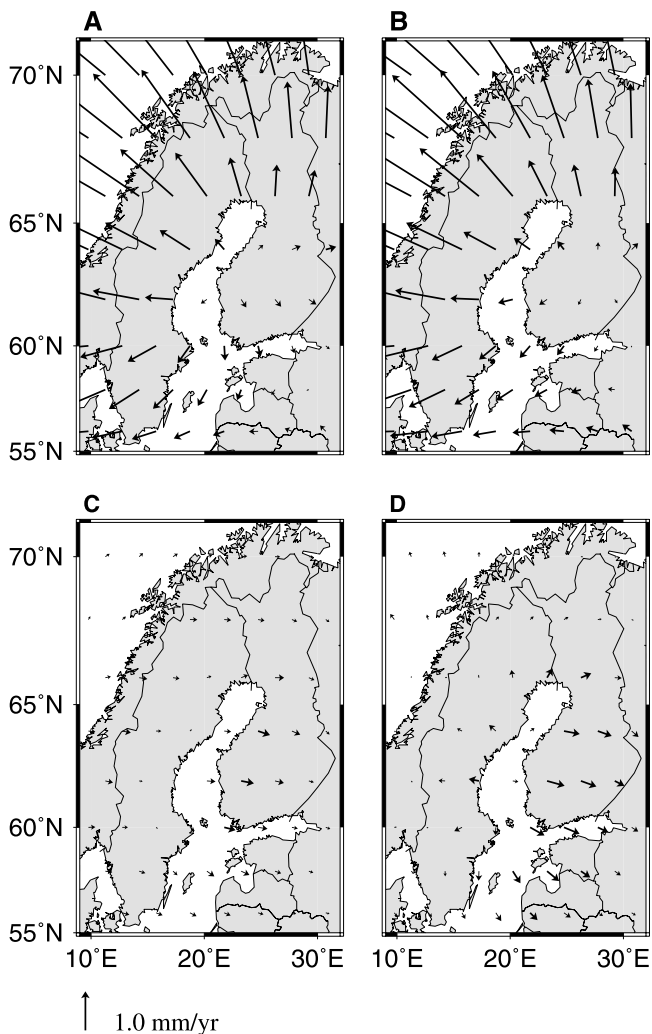
**Figure 4.** Analogous to the predictions shown in Figure 2 except that the present-day horizontal deformation rate field is shown. The GPS site locations are not shown. The scale vector is shown at the bottom left.

Figure 3b represents the ocean load change predicted over the preceding time step (from 11.6 to 10.2 ka), and so on. Between 11.6 and 10.2 ka, a large section of the gulf becomes ice free (Figure 3, left), and the new sea level theory correctly predicts an inundation of water into this region. The color contours on Figure 3 indicate that inundation extends over a broad swath of Finland and a portion of Sweden, indicating that these areas were below sea level (due to the crustal lowering caused by the ice load) at the time of ice retreat. The amplitude of the inundation reaches in excess of 400 m in the central portion of the gulf. Over the same period, the Baltic Sea to the south experiences a reduction in the ocean load of amplitude tens of meters. This region became ice free at an earlier stage in the model; hence, from 11.6 to 10.2 ka the predicted reduction in ocean load is primarily a consequence of continuing postglacial uplift of the local crust. In the next time slice, from 10.2 to 8.8 ka, the ice sheet disappears, and the northern tip of the Gulf of Bothnia is finally exposed. The corresponding ocean load prediction (Figures 3c, middle) shows an influx of water into this small area of ~200 m amplitude. During

the same period the remainder of gulf (i.e., the region that became ice free in the penultimate time step) experiences a significant reduction in the ocean load. This reduction is largely due to the postglacial uplift of the region; however, there is also a significant contribution from the fall in the ocean surface associated with the decreasing gravitational attraction of the ablating ice mass.

[19] The inundation of water into a region vacated by ablating ice is governed by the total distance between the geoid and solid surfaces in the region exposed by the ice retreat. In traditional postglacial sea level theory, the local water load is governed not by the total distance between the geoid and solid surfaces, but rather by changes in the height of each of these surfaces over the previous time step; hence the inundation process cannot be modeled. To illustrate this, Figure 3 (right) shows a sequence of predictions analogous to Figure 3 (middle), with the exception that the traditional theory for ocean load changes is applied. In this case, regions subject to recent ice retreat do not show an influx of water load. Instead, both crustal uplift and the changing gravitational attraction of the ablating ice mass lead to a reduction in the distance between the geoid and solid surfaces and thus a reduction in the local ocean load. Note that the two theories (Figures 3, middle, and 3, right) show relatively consistent predictions in regions that are not vacated by ice in the most recent time step.

[20] The results in Figure 3 indicate that the original sea level theory yields a considerably larger negative water load for the region compared to the revised theory. Figure 2d shows the ocean load signal in radial crustal velocity predicted on the basis of the original sea level equation. The predicted uplift signal is 2−3 times greater than that predicted using the revised theory in the vicinity of the Gulf of Bothnia (see Figure 2c). The error incurred by adopting the original sea level theory is as high as 1.6 mm/yr at the BIFROST sites, a discrepancy which exceeds the typical observational error.

[21] Figure 4 shows results that are analogous to those in Figure 2, with the exception that we now treat the horizontal deformation field. The total predicted signal (Figure 4a) displays the characteristic pattern of divergent motion centered near the location of the peak present-day uplift (and peak ice height at Last Glacial Maximum). This prediction is in accord with the general form of the observations (Figure 1c). The asymmetry in the predicted deformation pattern is largely a result of the deformation associated with the deglaciation of the distant Laurentide ice complex [*Mitrovica et al.*, 1994b]. As in Figure 2, the ice-load-induced signal generally dominates the total field. An exception to this rule is evident in southern Finland, where the magnitude of the ocean load signal is comparable to the horizontal motions produced by the ice loading. The error incurred by adopting the traditional sea level theory is most pronounced in the same region.

[22] Next we focus on deformation driven by GIA-induced perturbations in Earth rotation. The geometry of the perturbation to the centrifugal potential is described (to better than ~1%) by a degree 2 order one surface spherical harmonic [e.g., *Han and Wahr*, 1989; *Mitrovica et al.*, 2001]. The orientation of this potential forcing is governed by the GIA-induced polar wander path during the postglacial period, which lies, approximately, on the great circle
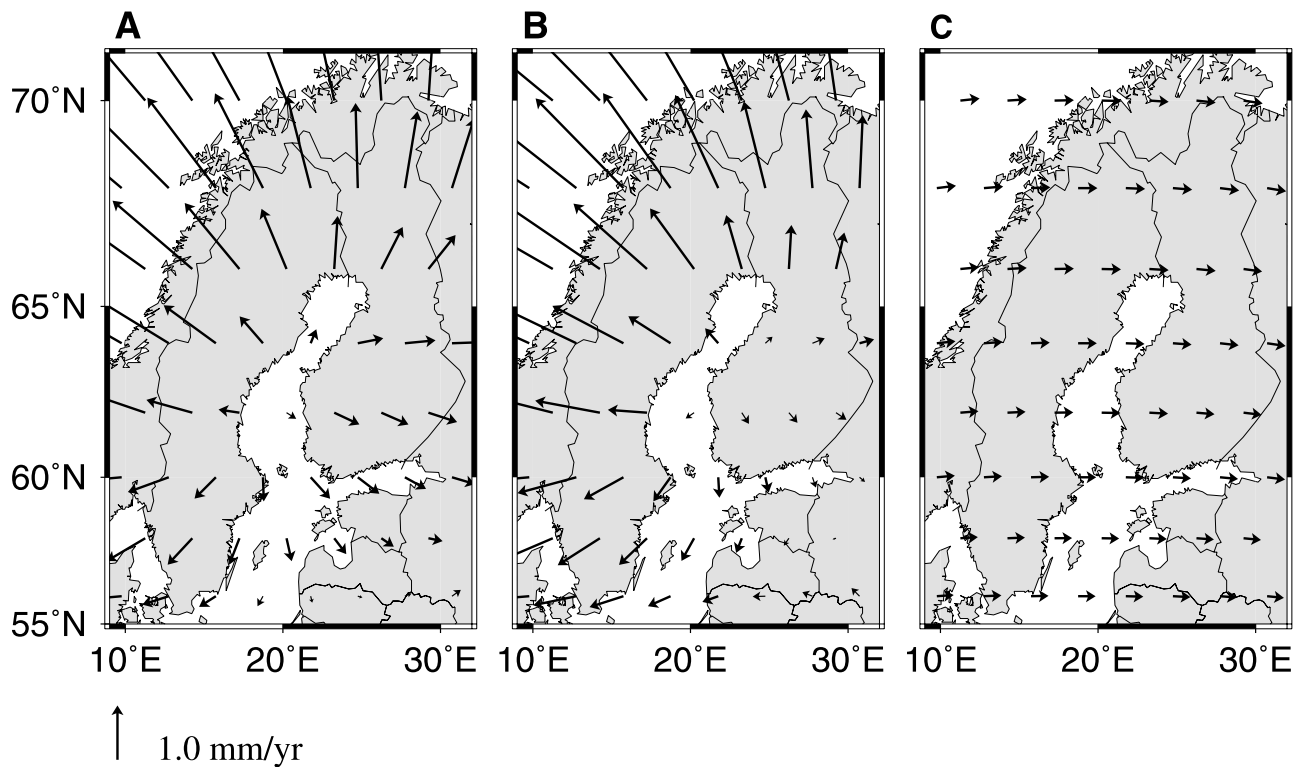
**Figure 5.** Predictions of the present-day horizontal crustal velocity field due to (a) both the GIA surface mass loading and the rotational potential, (b) the surface mass load only, and (c) the rotational potential only. Scale vector is at the bottom left.

(74°W, 106°E) [*Mitrovica et al.*, 2001]. Specifically, the perturbing rotational potential induced by this polar motion is a maximum along this great circle at midlatitudes, with nodes along the equator, the poles, and along the great circle of longitude oriented 90° east or west of the pole path.

[23] The radial component of the rotation-induced deformation field shares the same spatial signature as the rotational potential itself (see equations (A5) and (A8)). Thus the rotation-induced signal in Fennoscandia is not significant since this region is located approximately 90° east of the great circle defined by the polar wander path. In contrast, the horizontal deformation field has a geometry defined by the (spatial) gradient of the rotational potential (see equations (A6) and (A9)). Accordingly, the horizontal deformation field is relatively large in Fennoscandia [see also *Mitrovica et al.*, 2001]. In Figure 5 we decompose the total predicted horizontal velocity (Figure 5a) into the signal associated with a nonrotating Earth (Figure 5b, which is identical to Figure 4a) and the signal associated with rotation. The latter signal is relatively uniform within Fennoscandia, which reflects the broad spatial scale of the rotation signal, and it is directed west to east with a magnitude of ~0.4 mm/yr. It is clear that rotational effects have a significant impact on the predicted deformation pattern; for example, these effects act to counter the asymmetry introduced in Figure 5b from Laurentide deglaciation. In any event, the magnitude of the rotation signal exceeds the observational error (see Figure 1 and paper 1).

[24] The postglacial rebound literature includes a number of inferences of ice history and Earth model pairings based on analyses of sea level data. In Figure 6 we compare results of two such pairings with the intent to examine the sensitivity of the predictions to different ice histories as well as to determine which of these two published models provides the best fit to the data. In Figure 6a (top) we replot the prediction of present-day radial crustal velocity based on the Fennoscandian ice history of *Lambeck et al.* [1998a] and the Earth model specified above. This model produces an uplift pattern that reaches a maximum of 10.2 mm/yr between the sites Umeä and Skellefteä. The geometry of the velocity field reflects the spatial extent and the deglaciation history of the ice model: specifically, the LSJ model produces an oval-shaped pattern with the long axis trending, approximately, north-northeast to south-southwest. The results shown in Figure 6a (bottom) were generated using the ICE-3G model [*Tushingham and Peltier*, 1991] and the Earth model associated with this ice history; a lithospheric thickness of 120 km, upper mantle viscosity of $10^{21}$ Pa s, and a lower mantle viscosity of $2 \times 10^{21}$ Pa s (this ice-Earth model combination is hereinafter referred to as TP). The uplift pattern predicted by the TP model is distinct from the LSJ-based calculation: the center of uplift is located further to the east, and the signal displays an axis of symmetry that is aligned approximately northeast to southwest, with the region of uplift broadening toward the northeast. The maximum uplift rate for this ice-Earth model pair is 11.1 mm/yr.

[25] The results shown in Figure 6b are identical to those shown in Figure 6a, with the exception that the plotted fields are based only on the model results evaluated at the set of BIFROST station locations. These images can be compared directly to the observations (Figure 1b). In
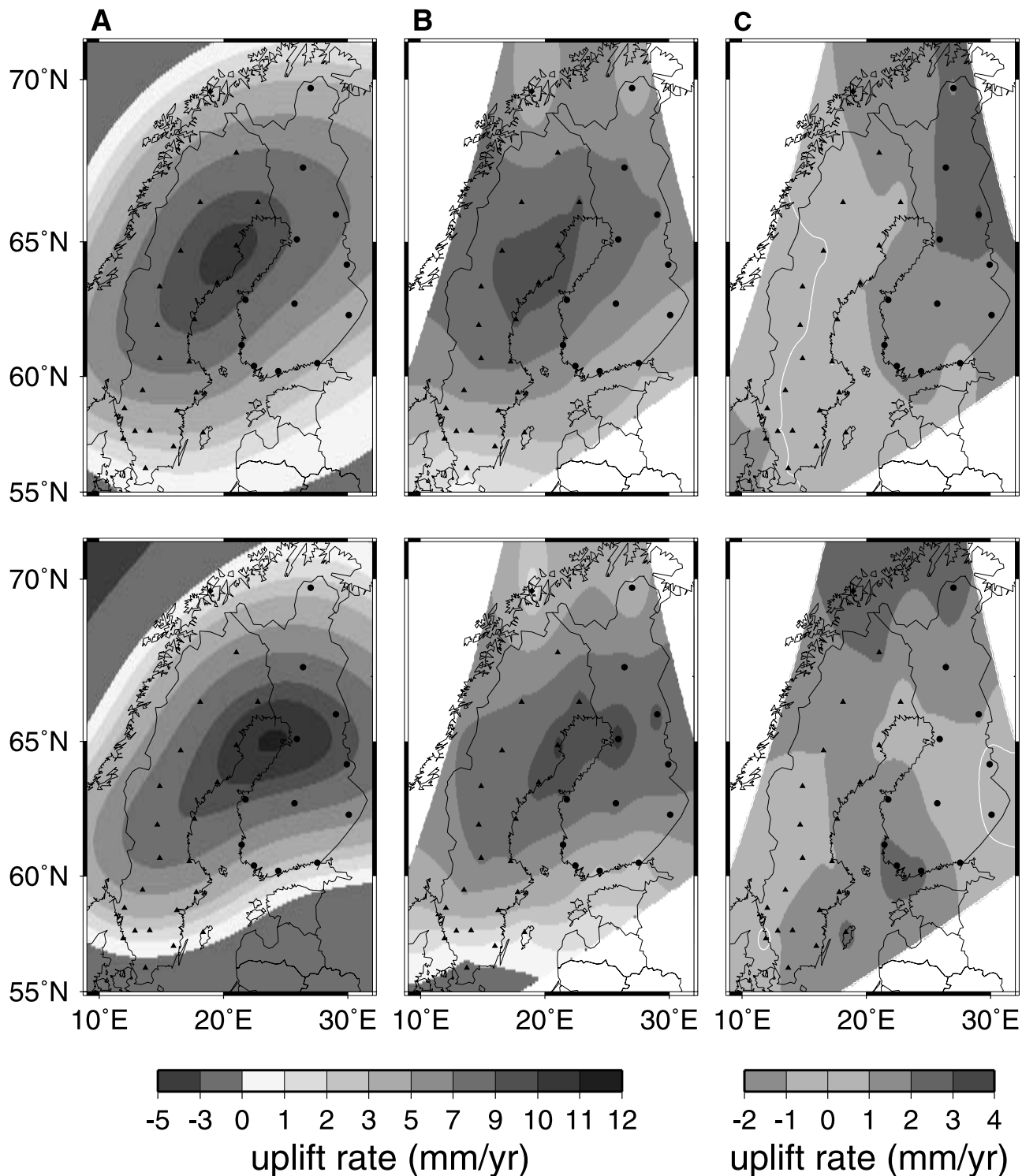
**Figure 6.** (a) Predictions of the present-day radial velocity field based on the (top) LSJ and (bottom) TP ice-model pairs (see text for details). (b) Same as in Figure 6a except that the predicted deformation field is sampled at GPS site locations only. These maps can be compared directly to observational results in Figure 1a. (c) Residual vertical deformation field calculated by subtracting the predicted rates from the observed rates. The zero contour is marked by a white line.

general, the pattern shown in Figure 1b (top) more closely matches the observations. The greatest misfit between the observations and the LSJ model is apparent in the northeast section of the plotted region (Figure 6c, top), where the

observed radial rates are underpredicted. However, note that the observations in this region exhibit the largest uncertainty. The TP model produces uplift contours that are oriented more east-west than north-south and so it does not, in
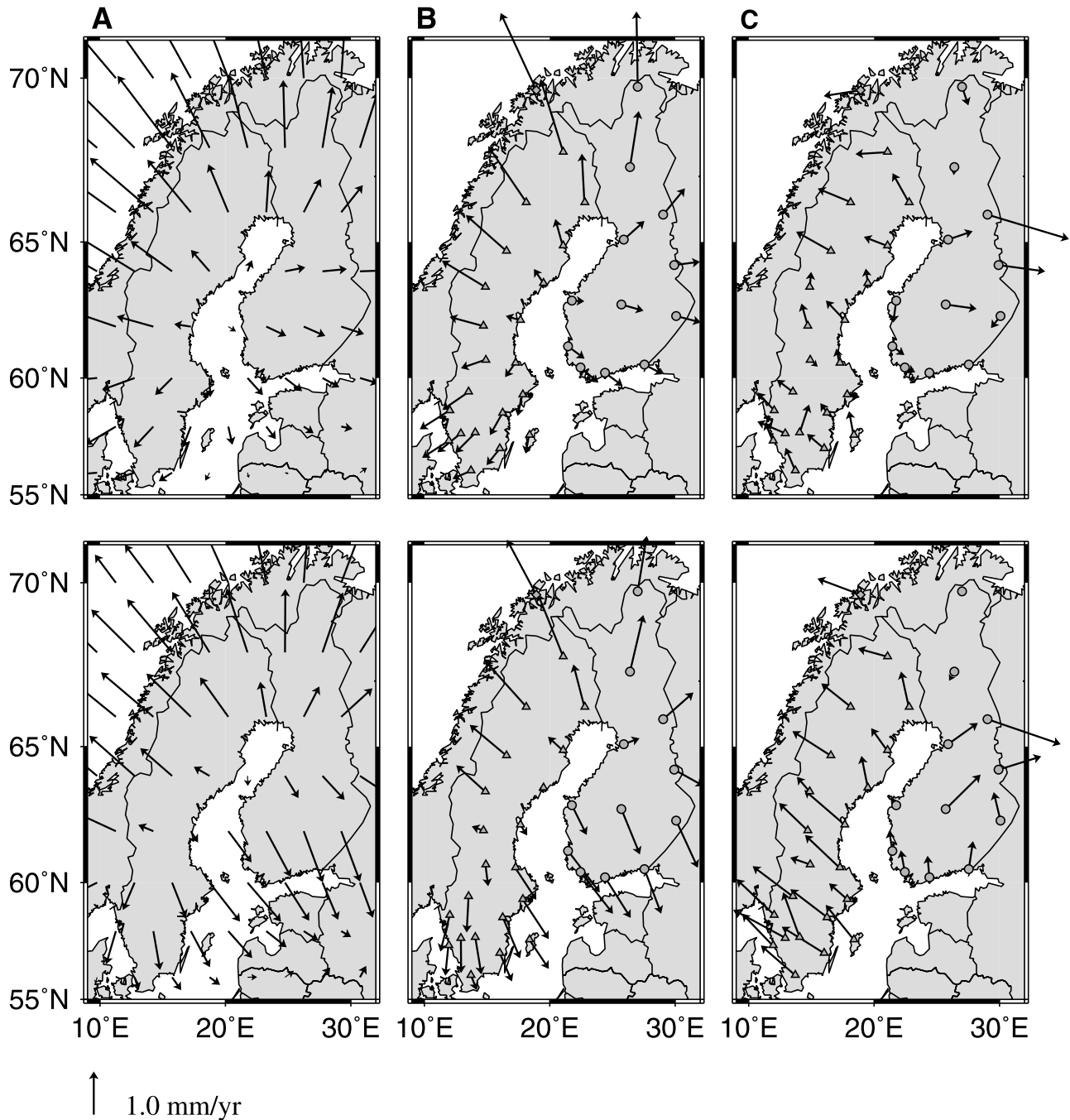
**Figure 7.** As in Figure 6, except that results for horizontal rates are shown. The vector magnitude scale is shown at bottom left.

general, produce a good match to the observations (Figure 6c, bottom). These qualitative comments are supported by the normalized $\chi^2$ misfit computed for these models: 5.94 and 10.3 for the LSJ and TP models, respectively. The $\chi^2$ values are computed by evaluating the observed rate minus the predicted rate divided by the observed error at each site, squaring this value and then summing the contributions for each site. This sum is then normalized by the number of observations minus one.

[26] Figure 7 shows an analogous plot of the predicted horizontal rates. Once again, the patterns of present-day horizontal velocity generated for the two models are distinct.

These differences are most apparent in the lower section of the map. For example, the TP model produces larger southward motion in southern Finland and southern Sweden. Comparison of the predictions in Figure 7b with the observations (Figure 1c) indicates that the latter is better matched by the LSJ model (see also column Figure 7c). The $\chi^2$ values for the LSJ and TP models are 16.8 and 30.6, respectively.

[27] It is interesting to note that the $\chi^2$ values for the fits to the horizontal rates are ∼3 times larger than those for the vertical rates. As discussed previously by *Milne et al.* [2001], this could be a result of limitations in the forward model due to, for example, a simplified 1-D Earth structure

or inaccuracies in the adopted ice model. These limitations have been shown to impact the predictions of horizontal rates more so than vertical rates [*Mitrovica et al.*, 1994b; *Wahr and Davis*, 2002]. With regard to the suggestion of uncertainties in the ice model, it is important to note that both of the ice models we have adopted were constrained using observations of relative sea level changes, which are directly affected by vertical crustal motion but are independent of horizontal motion. This suggests that inaccuracies in the ice models may be an important source of this variation in the $\chi^2$ values. Of course, the poorer fit to the horizontal rates could also be attributed to an underestimation of the true uncertainty in the horizontal rates.

[28] We next present the results of a detailed forward modeling analysis based on the LSJ ice history. In particular, we have predicted the Fennoscandian 3-D crustal deformation using this history and a large suite of Earth models in which the lithospheric thickness, upper mantle viscosity ($\nu_{UM}$) and lower mantle viscosity ($\nu_{LM}$) were varied over the ranges shown in Figure 8. For each of these runs we computed the normalized $\chi^2$ statistic and the results are shown in Figure 8.

[29] Figure 8a shows the results for the case in which only the vertical component of the rates is considered. There is significant trade-off between viscosity values in the upper and lower mantle. Consider, for example, the results for the case of a 120 km thick lithosphere: $\chi^2$ values of less than five can be achieved with an approximately isoviscous mantle of $\sim$2–3 $\times$ $10^{21}$ Pa s or with a two layer structure characterized by an order of magnitude jump in viscosity across the 670 km interface ($\nu_{UM} \sim 5 \times 10^{20}$ Pa s, $\nu_{LM} \sim 5$–$10 \times 10^{21}$ Pa s). A similar trade-off has been identified in inferences based on relative sea level data [e.g., *Lambeck et al.*, 1990; *Mitrovica*, 1996]. An important feature of the results for vertical rates is the rapid increase in the misfit as the upper mantle viscosity is reduced below about 5 $\times$ $10^{20}$ Pa s for lower mantle viscosity values ranging from 3 to 50 $\times$ $10^{21}$ Pa s. This gradient is a consequence of the marked decrease in the predicted present-day uplift rates as the upper mantle viscosity is reduced below this threshold. For such viscosity models, the relatively rapid isostatic uplift has yielded relatively small levels of remnant (i.e., present-day) disequilibrium.

[30] Figure 8b shows the $\chi^2$ results when only the horizontal component of the rates is taken into account. Since the GIA model does less well in predicting the horizontal rates compared to the vertical rates (see Figure 7 and related discussion), the error bars for these data were scaled by a factor of 1.8 to produce a minimum $\chi^2$ value that matches that for the vertical rates. This scaling of the error in the horizontal rates was performed as a preliminary attempt to account for the influence of uncertainties in the ice model. In Figure 8b the region of viscosity space where the best fit is achieved is significantly different from the location of the minimum in Figure 8a. In particular, upper mantle viscosities greater than $\sim$$10^{21}$ Pa s, and lower mantle viscosities less than $\sim$3 $\times$ $10^{21}$ Pa s are excluded on the basis of the horizontal velocities. Thus, when considering misfit for the combined horizontal and vertical motions (Figure 8c), a relatively small region of acceptable viscosity model space is isolated. We conclude that horizontal motions provide constraints on viscosity which are distinct

from those provided by observations which reflect vertical deformation (radial crustal uplift rates, sea level changes).

[31] Figures 8 (top), 8 (middle), and 8 (bottom) refer to a different value for the adopted lithospheric thickness. (Our calculations were extended to include lithosphere thicknesses of 146 km and 171 km, but these results are not shown.) The model with a lithospheric thickness of 120 km was found to produce the minimum $\chi^2$ value (for $\nu_{UM} = 8 \times 10^{20}$ Pa s and $\nu_{LM} = 10^{22}$ Pa s).

[32] Applying an *F* test to the results shown in Figure 8c (bottom), yields the following 95% confidence interval: 5 $\times$ $10^{20} \leq \nu_{UM} \leq 10^{21}$ Pa s; 5 $\times$ $10^{21} \leq \nu_{LM} \leq 5 \times 10^{22}$ Pa s.

[33] In Figure 9 the $\chi^2$ results are plotted as a function of lithospheric thickness and $\nu_{UM}$ for a fixed $\nu_{LM}$ value of $10^{22}$ Pa s. In this case, the radial rates show a relatively weak correlation between lithospheric thickness and upper mantle viscosity, while a strong trade-off is evident in the fits to the horizontal rates. In regard to the latter, the quality of fit can be maintained by increasing or decreasing both parameters simultaneously within a given parameter range. As an example, a good fit can be obtained for either a relatively thick lithosphere ($\sim$140 km) and high $\nu_{UM}$ ($\sim$$10^{21}$ Pa s), or a relatively thin lithosphere ($\sim$80 km) and low $\nu_{UM}$ ($\sim$5 $\times$ $10^{20}$ Pa s). As we noted in the context of Figure 8, the vertical rates cannot be fit for $\nu_{UM}$ less than $\sim$5 $\times$ $10^{20}$ Pa s (regardless of the value adopted for lithospheric thickness) and the 3-D rates prefer a relatively thick lithosphere, with a 95% confidence interval of 90 to 170 km.

[34] The optimum parameter ranges cited above are broadly consistent with other inferences of mantle viscosity based on GIA data from Fennoscandia. Using geological records of postglacial sea level change, *Lambeck et al.* [1998a] inferred values of lithospheric thickness (65–85 km) and upper mantle viscosity (3–4 $\times$ $10^{20}$ Pa s) which lie at the lower bound of our ranges. A companion study based on instrumented sea level records [*Lambeck et al.*, 1998b] yielded slightly higher values for both these parameters (80–100 km and (4–5) $\times$ $10^{20}$ Pa s). *Wieczerkowski et al.* [1999] have used their newly derived estimate of the Fennoscandian relaxation spectrum to infer a mean viscosity within the bulk of the sublithospheric upper mantle of $\sim$5 $\times$ $10^{20}$ Pa s; this is also near the lower bound of our inferred range. Most recently, *Kaufmann and Lambeck* [2002] inverted a wide subset of GIA data, including relative sea level histories from Fennoscandia, and derived bulk upper and lower mantle values (7 $\times$ $10^{20}$ Pa s, 2 $\times$ $10^{22}$ Pa s, respectively) near the center of our preferred ranges.

[35] We next investigate the influence of the choice of ice model on the inference of Earth model parameters. In Figure 10 we repeat the calculations of Figure 8 (for a lithospheric thickness of 120 km) using the ICE-3G deglaciation history discussed above. The general location and structure of the $\chi^2$ minimum in viscosity space is similar to that obtained with the LSJ model, although the $\chi^2$ values are consistently higher for the ICE-3G predictions. We conclude that our choice between these two ice models does not significantly influence the inferred range of optimum Earth model parameters. It is interesting to note that the specific Earth model used in the derivation of the ICE-3G load history (LT = 120 km, $\nu_{UM} = 10^{21}$ Pa s,
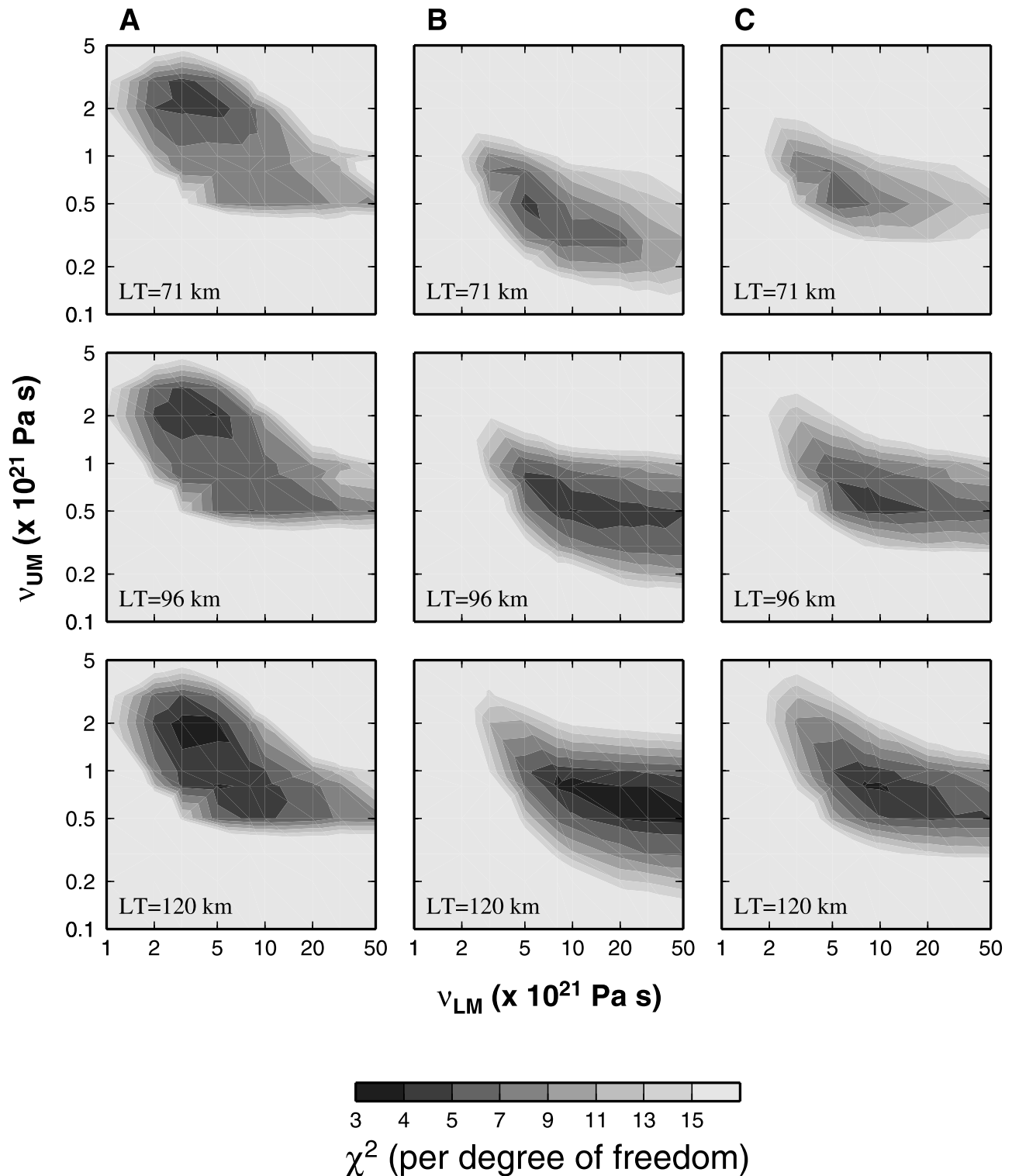
**Figure 8.** Normalized $\chi^2$ contour plots for a variety of Earth models characterized by an elastic lithosphere of thickness 71, 96 or 120 km (see label at bottom left) and a two-layer sublithospheric mantle viscosity with a range of uniform values within the upper mantle ($\nu_{UM}$) and lower mantle ($\nu_{LM}$) regions. Results are shown for (a) vertical rates only, (b) horizontal rates only, and (c) all three rate components.

$\nu_{LM} = 2 \times 10^{21}$ Pa s) does not yield a good fit to the 3-D rates in Fennoscandia.

[36] The forward modeling analysis presented above and the inverse analysis presented below are based on single-site position estimates for each of the BIFROST stations. The rates based on these time series may be systematically biased due to perturbations in both the reference frame realizations and the satellite orbits during the monitoring
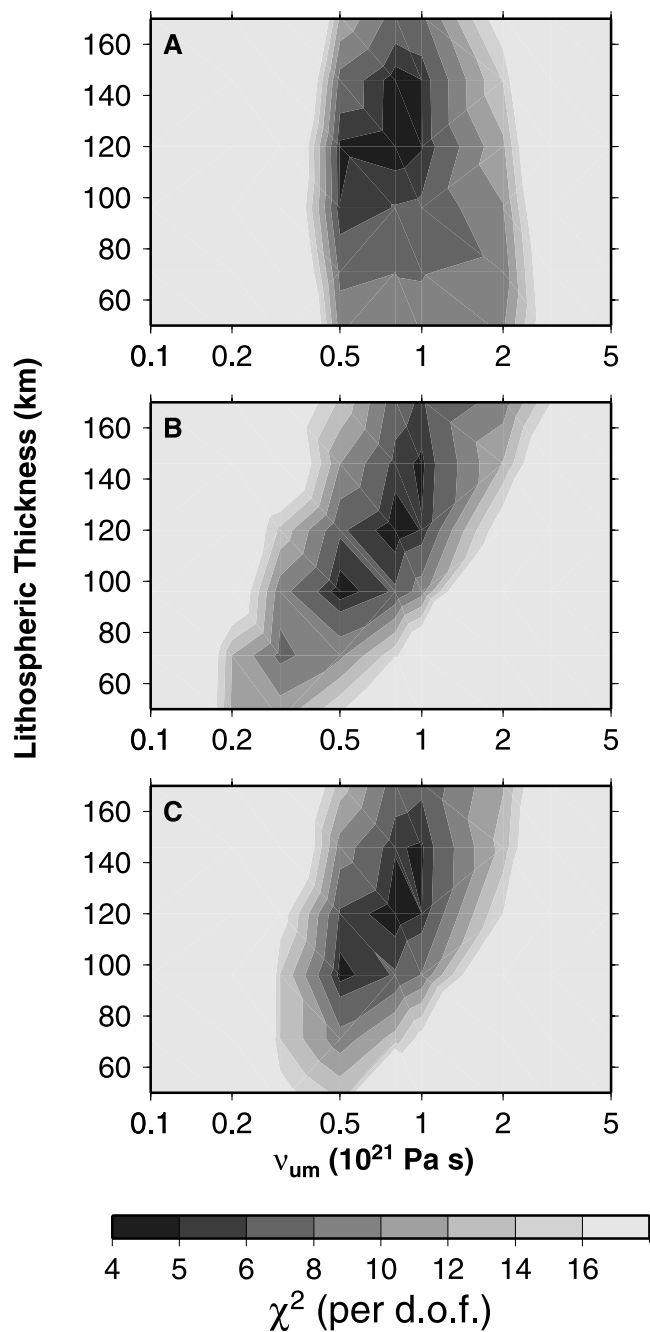
**Figure 9.** Normalized $\chi^2$ values plotted as a function of lithospheric thickness and upper mantle viscosity ($\nu_{UM}$) for a fixed lower mantle viscosity of $10^{22}$ Pa s. As in Figure 8, results are shown for (a) vertical rates only, (b) horizontal rates only, and (c) all three rate components.

period. The error would appear as a long-wavelength feature in the observed 3-D velocity field. A related point in this regard is the difficulty in separating long-wavelength contributions to the horizontal motion associated with GIA (e.g., the rotation-induced signal (Figure 5c) or that due to the distant Laurentide ice sheet [*Mitrovica et al.*, 1994b]) from that associated with the rigid component of tectonic plate motion.

[37] We have performed a regional strain rate analysis using the BIFROST data to investigate the influence of

these issues on the accuracy of our viscosity inference (S. Bergstrand et al., Upper mantle viscosity from continuous GPS baselines in Fennoscandia, submitted to *Journal of Geodynamics*, 2003). This type of analysis is less sensitive to long-wavelength signals in the observed velocity field. The results based on the strain rate analysis give a 95% confidence range for $\nu_{UM}$ of $3-10 \times 10^{20}$ Pa s and an
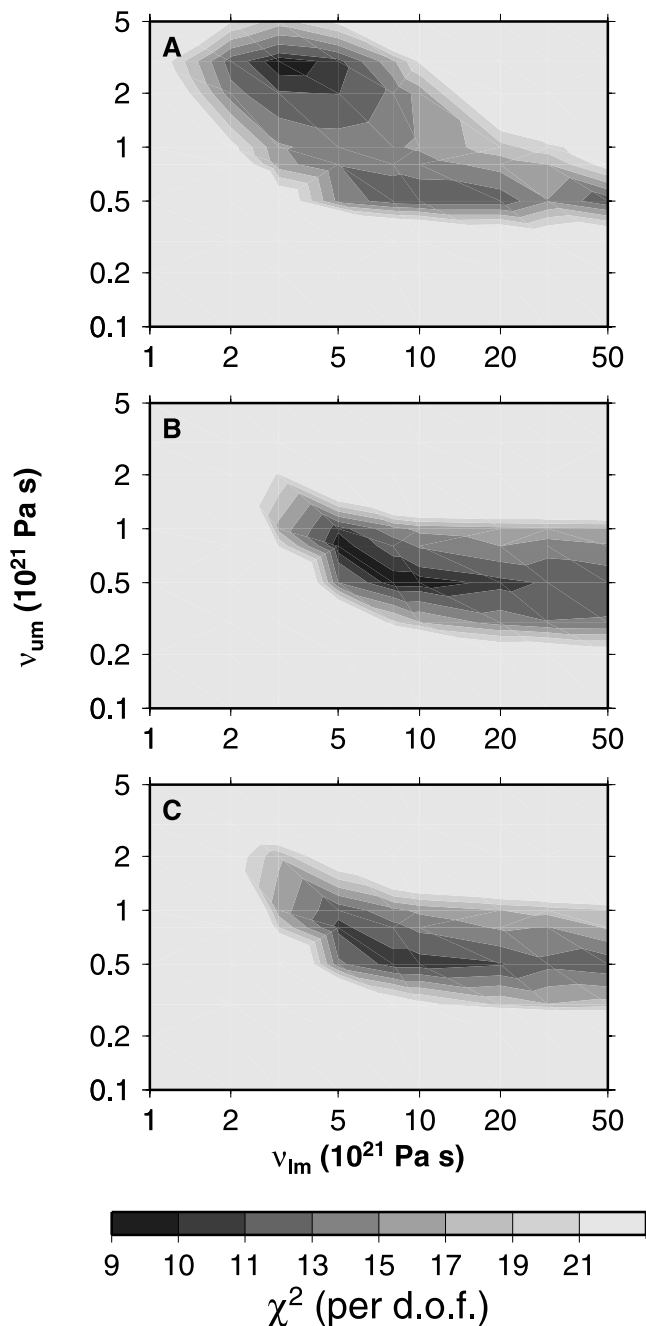


**Figure 10.** Normalized $\chi^2$ contour plots based on the ICE-3G deglaciation model for a variety of Earth models characterized by an elastic lithosphere of thickness 120 km and a two-layer sublithospheric mantle viscosity with a range of uniform values within the upper mantle ($\nu_{UM}$) and lower mantle ($\nu_{LM}$) regions. Results are shown for (a) vertical rates only, (b) horizontal rates only, and (c) all three rate components.

optimum lithospheric thickness of 120 km, in agreement with our present results.

### 3.2. Inverse Analysis

[38] The forward analyses summarized in Figures 8–10, although an extension of earlier work [*Milne et al.*, 2001], provide a rather coarse measure of the sensitivity of the BIFROST data to variations in mantle viscosity. As a simple example, the correlation between values of $\nu_{UM}$ and $\nu_{LM}$ in Figure 8 preferred on the basis of radial velocity data suggest that these data do not independently resolve the bulk upper and lower mantle viscosity. This point is part of a broader question that serves as the focus of the present section; namely, what is the radial resolving power of the BIFROST data set?

[39] To answer this question, we perform a joint inversion of the BIFROST data set of present-day 3-D crustal velocities. For this purpose we adopt a Bayesian inference procedure. As in previous work on the viscosity problem, we parameterize the inversion in terms of the logarithm of viscosity in a set of discrete layers [e.g., *Mitrovica and Forte*, 1997]. In this regard, the "model" to be inverted for also includes a final parameter equal to the thickness of the elastic lithosphere, and we can thus write

$$\hat{X} = \left[\log \nu(r_j) \quad \text{for} \quad j = 1, N-1; LT\right], \qquad (1)$$

where $j$ denotes the radial layer ($j = 1$ is the layer above the core-mantle boundary, and $j = N - 1$ is the layer below the elastic lithosphere) and LT is the lithospheric thickness (nondimensionalized using the radius of the Earth, $a$). The model $\hat{X}$ has a total of $N$ parameters.

[40] We have chosen to discretize the mantle viscosity into a set of 22 uniform layers, with 9 residing within the lower mantle. Thus $N = 23$. The inverted model is specified by both the a posteriori model and covariance matrix. The diagonal elements of the latter provide the variances of the 23 individual model parameters. The BIFROST data will not be capable of resolving structure on the length scale of the individual viscosity model layers, and therefore the a posteriori variances for these model estimates will not be substantially smaller than the prior variances adopted in the inversions (we have found that the greatest reduction is of the order 30–40%). We will estimate the resolving power of the BIFROST data by examining the posterior covariance matrix. The spread of the off-diagonal elements for, say, the $j$th row of this matrix provides a measure of the radial resolving power of the data for an estimate of viscosity at a depth corresponding to the $j$th radial layer [e.g., *Tarantola and Valette*, 1982]. As we note below, the a posteriori uncertainty for an estimate of the average viscosity over this resolving width will, in contrast to the uncertainty for an individual model value, be significantly smaller than the prior uncertainty.

[41] The prior and starting model for our inversion corresponds to an Earth model with an elastic lithosphere of 96 km, an upper mantle viscosity of $5 \times 10^{20}$ Pa s, and a lower mantle viscosity of $5 \times 10^{21}$ Pa s. The Fréchet kernels are computed numerically using a suite of models in which the viscosity in the 22 mantle layers and the lithospheric thickness are perturbed from the values defining this starting

model. As an illustration, we show, in Figure 11, Fréchet kernels for the prediction of the three components of crustal velocity for a set of eight sites lying (south to north) along the major axis of the Fennoscandian deformation region (see Figure 1a for site locations). To account for differences in the thickness of the radial layers, each plotted value of the kernels has been normalized by the (nondimensional) thickness of the associated radial layer. Since the predictions have a nonlinear dependence on mantle viscosity, the kernels will be a function of the model; nevertheless, the starting model was adopted because it provides a near best fit to the BIFROST-derived estimates of 3-D crustal velocity (Figure 8c).

[42] The Fréchet kernels provide a measure of the detailed depth-dependent sensitivity of a particular datum to variations in the radial profile of mantle viscosity. Predictions of radial velocity for sites within central Fennoscandia (Mårtsbo to Sodankylä) based on the starting model show a broad sensitivity to bulk upper mantle viscosity. Significant changes in this pattern of sensitivity are evident as one considers sites closer to the perimeter of the Fennoscandian ice complex at Last Glacial Maximum, Hässleholm to the south and Kevo to the north. With the possible exception of Hässleholm, all predictions of radial velocity show a moderate, but nonnegligible sensitivity to variations in lower mantle viscosity (at least in the shallowest portions of this region), and this explains the trade-off evident in Figure 8a.

[43] The predictions of horizontal velocity show a distinct sensitivity to variations in the mantle viscosity profile. These predictions have a sensitivity that tends to peak near the top of the mantle. Furthermore, while there is little sensitivity to variations in viscosity within the top half of the lower mantle, a nonzero sensitivity is apparent at some sites (e.g., Jönköping) near the base of the mantle.

[44] Figure 12 shows the results of two inversions of the BIFROST data set. For each of these inversions the dotted line on Figure 12 represents the prior (and starting) viscosity model. The dashed line is the posterior model for a preliminary inversion in which the viscosity in layers within the lower and, independently, the upper mantle, are assumed to be perfectly correlated; this assumption yields a two-layer viscosity model characterized by $\nu_{LM} \sim 10^{22}$ Pa s and $\nu_{UM} \sim 5.5 \times 10^{20}$ Pa s, and lithospheric thickness of $\sim$116 km. We note, in reference to Figure 8c, that this model falls close to the best fit model determined by our forward analysis.

[45] The solid line on Figure 12 shows the radial viscosity profile generated from a multilayer inversion of the BIFROST data set. In the upper mantle, this model oscillates around the starting/prior model (with the exception of a thin layer of low viscosity at the base of the lithosphere). In addition, the model trends toward values in excess of $10^{22}$ Pas in the top half of the lower mantle before returning to a viscosity close to the prior value near the base of the mantle. (The posterior estimate of lithospheric thickness in this inversion is $104 \pm 6$ km.)

[46] The question arises as to whether these variations in the viscosity are actually resolved by the BIFROST data set. To answer this question, we turn to Figure 13, which provides plots of the off-diagonal elements of the covariance matrix for eight target depths (i.e., depths corresponding to a specific layer of the model) ranging
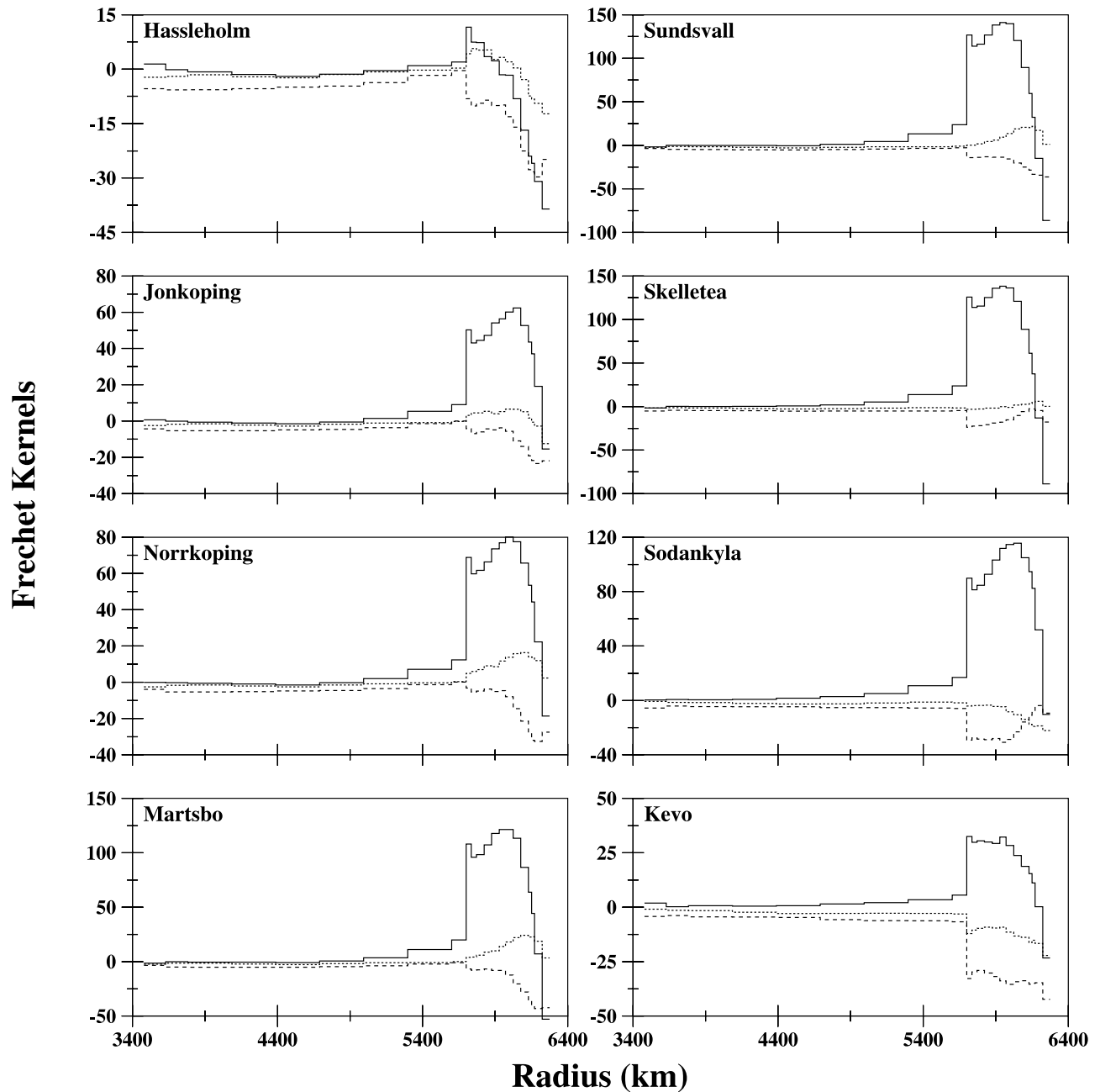
**Figure 11.** Fréchet kernels (see text) as a function of radius for predictions of the three components of present-day crustal velocity: solid line, radial; dashed line, horizontal south; dotted line, horizontal east. Each panel refers to a different site in the BIFROST GPS network (see Figure 1). Each value of the kernel is normalized by the (nondimensional) thickness of the associated radial layer in order to remove any sensitivity to layer thickness. The kernels each have 22 values, nine within the lower mantle and the remainder in the sublithospheric upper mantle. A 23rd value (not plotted or shown) used in the inversions refers to changes in the thickness of the elastic lithosphere. The kernels were computed for a starting model defined as having a lithosphere of thickness 96 km, $\nu_{UM} = 5 \times 10^{20}$ Pa s, and $\nu_{LM} = 5 \times 10^{21}$ Pa s.

from the shallow upper mantle to 1225 km depth. The individual plots are normalized by the largest off-diagonal value and the diagonal element (i.e., the variance) is not shown. Below target depths of ~1300 km we have noted that the location of the peak off-diagonal element is generally widely displaced from the target and this indicates that the BIFROST data do not provide significant radial resolution of mantle viscosity in this region of the lower mantle.

In contrast, at progressively shallower depths, Figure 13 indicates a resolving power which gradually improves.

[47] Let us, for the purpose of illustration, define the resolving width as the radial range of the off-diagonal elements having values equal to or greater than 50% of the peak off-diagonal value (i.e., width at half max). In this case, the radial resolving power of the BIFROST data at the target depth of 230 km is ~200 km. This resolving power
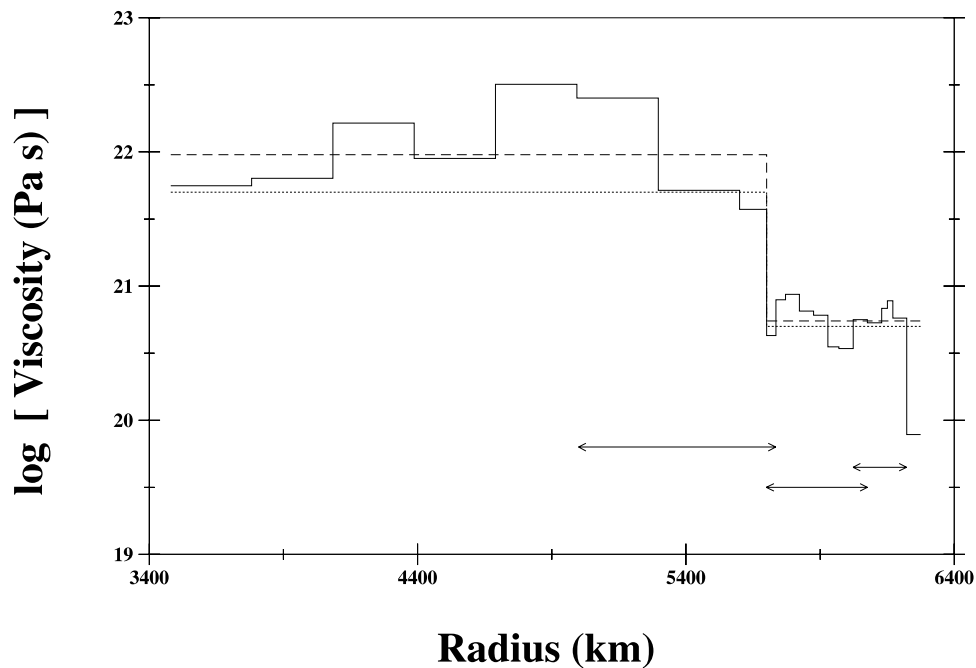
**Figure 12.** Results of a Bayesian inversion of the BIFROST GPS data set. The dotted line represents the starting and prior (two layer) viscosity model adopted in the inversion ($\nu_{UM} = 5 \times 10^{20}$ Pa s, $\nu_{LM} = 5 \times 10^{21}$ Pa s); the starting lithospheric thickness is 96 km. The dashed line is the inverted profile generated by assuming that the layers in the upper and (independently) the lower mantle are perfectly correlated (posterior LT = 106 km). The solid line shows the results for a full multilayer inversion of the GPS data set (posterior LT = 103 ± 8 km). The off-diagonal elements for a subset of rows in the associated posterior covariance matrix is given in Figure 13. The three horizontal lines at bottom right illustrate three of the radial regions which are resolved by the BIFROST data set (see text and Figure 13).

reduces to ~380 km at a target depth of 468 km and ~640 km at 652 km depth. We can conclude, for example, that both the low-viscosity layer of thickness ~50 km at the base of lithosphere and the high viscosity hump at ~1400 km depth (solid line, Figure 12) are not resolvable by the BIFROST data. Furthermore, while target depths ranging from 800 to 1300 km show relatively little covariance with upper mantle viscosity values, some sensitivity to upper mantle structure is always evident; this is in accord with the forward results in Figure 8c.

[48] In Figure 12 we show three radial regions (bottom right) which are, according to Figure 13, resolvable by the BIFROST data. From deepest to shallowest, the weighted (by the resolving kernel) mean of the viscosity profile within these regions is: $8.9 \times 10^{21}$ Pa s, $5.4 \times 10^{20}$ Pa s, and $5.9 \times 10^{20}$ Pa s, respectively. Over depth ranges resolvable by the BIFROST data, the observational constraints lead to an order of magnitude reduction in the variance of the averages.

## 4. Final Remarks

[49] The BIFROST Fennoscandian GPS network was the first to produce maps of the present-day, 3-D crustal velocity field associated with GIA. In a general sense, these maps confirmed the basic postglacial deformation pattern first predicted theoretically in the early 1990s [*James and Lambert*, 1993; *Mitrovica et al.*, 1993, 1994b], namely, ongoing radial rebound of previously glaciated regions

and horizontal motions directed outward from the zone of maximum uplift. After roughly a decade of GPS data collection, the observational uncertainties in the rate estimates are now sufficiently small (Figure 1) that increasingly accurate theoretical predictions must be brought to bear to analyze the data. We have demonstrated, for example, that the signal associated with recent improvements in the GIA theory, for example the inclusion of crustal deformations driven by perturbations in the Earth's rotation vector and a refined treatment of the water load in the vicinity of an ablating ice margin and evolving shoreline, exceed the current observational uncertainty.

[50] The ability of modern numerical models of the GIA process to accurately reconcile the BIFROST rate estimates permits a wide number of geophysical applications [e.g., *Milne et al.*, 2001]. The forward analyses described herein touch upon two of the classic GIA analyses; namely, constraining the space-time history of late Pleistocene ice cover and the radial profile of mantle viscosity. Our results indicate that the BIFROST data provide a potentially powerful test for models of the ice history (Figures 6 and 7) and permit bounds to be placed on the bulk upper and (shallow) lower mantle viscosity and the lithospheric thickness (Figure 8).

[51] Our analysis was completed by performing the first formal inversion of the BIFROST data set. The main goal of this inversion was a determination of the resolving power of the GPS estimates of 3-D crustal velocities. In this regard, the results in Figure 13 have several important implications
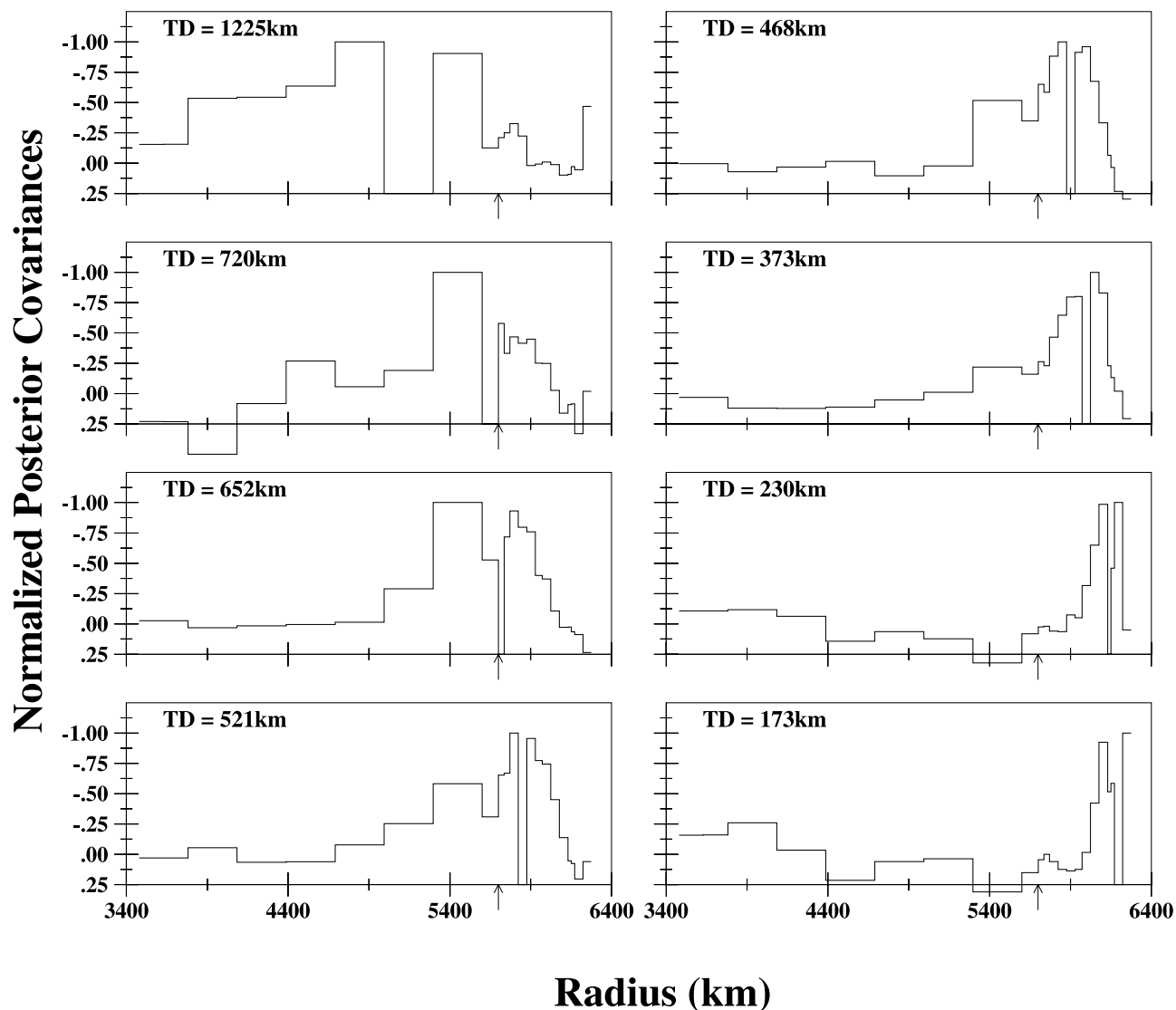
**Figure 13.** Plot of the off-diagonal elements for a set of eight rows in the posterior covariance matrix generated by Bayesian inversion of the BIFROST data set (the associated inverted model is given by the solid line in Figure 12). The values are normalized by the largest off-diagonal (i.e., covariance) in each case. The target depth (TD) is specified by the label on each panel, and it is located at the center of the layer whose value is not shown on the plot. The up-pointing arrow on the abscissa of each panel indicates the radius of the 670 km discontinuity marking the boundary between the upper and lower mantle.

for the forward analyses of mantle viscosity summarized in Figure 8. First, the inference of lower mantle viscosity implied by the analysis in Figure 8 is more accurately interpreted as a constraint on the viscosity in the top ∼800 km of this region. This limitation should not be surprising given the size of the Fennoscandian ice complex that covered the region at Last Glacial Maximum (see *Mitrovica* [1996] for a discussion). Furthermore, the BIFROST data are able to resolve structure on radial scales finer that the entire width of the upper mantle. Specifically, this resolution ranges from ∼200 km just below the lithosphere to ∼300 km near the base of the upper mantle. Accordingly, a significant improvement in the fit of the forward models may be achievable by considering a suite of models with two or three isoviscous layers within the upper mantle.

[52] As we have discussed, our inferences of viscosity within the upper mantle and the top portion of the lower mantle are reasonably consistent with previous studies based (at least in part) on the GIA record within Fennoscandia. We have inferred lower bounds of ∼5 × 10²⁰ Pa s on the bulk upper mantle viscosity below Fennoscandia and ∼90 km on the elastic thickness of the Fennoscandian craton. The resolving power of the data is not sufficient to rule out a thin low-viscosity region below the lithosphere; however, any region of significant weakness extending ∼200 km or more from the lithosphere does appear to be ruled out on the basis of the 3-D rates. The resolving power of the observations to depths of ∼1300 km will continue to improve as the BIFROST time series are extended and the observational error reduced further. Future analyses may therefore be able to provide more robust constraints on the

possible existence of a thin low viscosity region immediately below the Fennoscandian craton.

[53] In future work we plan to extend the above forward and inverse modeling analyses in three important ways. First, we will consider a revised GPS data set in which the rates will be based on time series that are several years longer than those considered here. Second, we will employ a series of ice histories that are generated from a realistic glaciological model and are validated with observational evidence from the regional geological record. Third, we will incorporate independent data sets in the inversions. These will include the so-called Fennoscandian relaxation spectrum [*McConnell*, 1968; *Wieczerkowski et al.*, 1999] and a set of postglacial decay times determined from central Fennoscandia [e.g., *Mitrovica and Forte*, 1997].

[54] The incorporation of lateral variations in Earth structure will also serve as a focus for future work. These variations, whether in the form of heterogeneities in lithospheric strength or mantle structure, are an area of active interest in GIA research [e.g., *Kaufmann and Wu*, 2002], and they will no doubt impact the prediction (and analysis) of the BIFROST GPS-determined rates. Members of the BIFROST Project have completed the development of a finite element numerical formulation of GIA on aspherical Earth models (K. Latychev et al., Glacial isostatic adjustment on 3-D earth models: A finite-volume formulation, submitted to *Geophysical Journal International*, 2003). The future application of this formulation to the present-day Fennoscandian deformation field will be an important extension of the work presented here.

## Appendix A: Theoretical Formalism for Computing 3-D Surface Deformation

[55] In the following, we provide a brief sketch of the spectral theory developed to calculate the three components of surface deformation associated with GIA. Computation of the impulse response of the (Maxwell) viscoelastic Earth model is based on a normal mode theory developed by *Peltier* [1974], *Peltier and Andrews* [1976], and *Wu* [1978]. This response is represented in terms of so-called viscoelastic Love numbers which, in the time domain, have the following form [*Peltier and Andrews*, 1976]:

$$h_\ell^L(t) = h_\ell^{L,E}\delta(t) + \sum_{j=1}^{J} r_j^{\ell,L} \exp\left(-s_j^\ell t\right), \tag{A1}$$

$$l_\ell^L(t) = l_\ell^{L,E}\delta(t) + \sum_{j=1}^{J} r_j'^{\ell,L} \exp\left(-s_j^\ell t\right), \tag{A2}$$

$$h_\ell^T(t) = h_\ell^{T,E}\delta(t) + \sum_{j=1}^{J} r_j^{\ell,T} \exp\left(-s_j^\ell t\right), \tag{A3}$$

$$l_\ell^T(t) = l_\ell^{T,E}\delta(t) + \sum_{j=1}^{J} r_j'^{\ell,T} \exp\left(-s_j^\ell t\right), \tag{A4}$$

where the superscripts $L$ and $T$ represent Love numbers for the case of a surface mass load (load Love numbers) and

gravitational potential forcing (tidal or tidal-effective Love numbers), respectively. The first term on the right-hand side of equations (A1)–(A4) denotes the instantaneous elastic response (hence the superscript $E$) to the associated forcing, while the second term is the nonelastic response. The latter is composed of a set of $J$ modes of pure exponential decay. The $h$ and $l$ Love numbers govern the radial and tangential displacement response, respectively, at spherical harmonic degree $\ell$. The adopted viscoelastic structure of the Earth model is embedded within these Love numbers.

[56] With these expressions in hand we can proceed toward a spectral formulation of the radial and horizontal crustal displacement responses due to GIA. Let us denote these responses as $R(\theta, \psi, t)$ and $\mathbf{V}(\theta, \psi, t)$, respectively, where $\theta$ is the colatitude, $\psi$ is the east longitude, and $t$ is the time. A spherical harmonic decomposition of these fields may be written as [*Mitrovica et al.*, 1994a, 2001]

$$R(\theta,\psi,t) = \sum_{\ell=0}^{\infty} \sum_{m=-\ell}^{\ell} R_{\ell,m}(t) Y_{\ell,m}(\theta,\psi) \tag{A5}$$

$$\mathbf{V}(\theta,\psi,t) = \sum_{\ell=0}^{\infty} \sum_{m=-\ell}^{\ell} V_{\ell,m}(t) \nabla Y_{\ell,m}(\theta,\psi), \tag{A6}$$

where $m$ is the spherical harmonic order, $\nabla$ is the two-dimensional gradient operator, and $Y_{\ell,m}$ is the surface spherical harmonic basis function. We adopt the specific normalization

$$\iint_\Omega Y_{\ell',m'}^\dagger(\theta,\psi) Y_{\ell,m}(\theta,\psi) \sin\theta \, d\theta d\psi = 4\pi\delta_{\ell',\ell}\delta_{m',m}, \tag{A7}$$

where the dagger denotes the complex conjugate and $\Omega$ represents the unit sphere.

[57] The GIA forcing is composed of contributions from the surface mass load and a gravitational potential perturbation (the so-called rotational potential) arising from GIA-induced changes in the planetary rotation vector. We denote the spherical harmonic coefficients of the former by $L_{\ell,m}$ and of the latter by $\Lambda_{\ell,m}$, respectively. The harmonic coefficients in the spectral decompositions (A5) and (A6) are then [e.g., *Mitrovica et al.*, 2001]

$$R_{\ell,m}(t) = \int_{-\infty}^{t} \left[ \frac{\Lambda_{\ell,m}(t')}{g} h_\ell^T(t-t') + \frac{4\pi a^3}{(2\ell+1)M_e} L_{\ell,m}(t') \right. $$
$$\left. \cdot h_\ell^L(t-t') \right] dt' \tag{A8}$$

$$V_{\ell,m}(t) = \int_{-\infty}^{t} \left[ \frac{\Lambda_{\ell,m}(t')}{g} l_\ell^T(t-t') \right. $$
$$\left. + \frac{4\pi a^3}{(2\ell+1)M_e} L_{\ell,m}(t') l_\ell^L(t-t') \right] dt', \tag{A9}$$

where $a$ and $M_e$ are the Earth's radius and mass, respectively, and $g$ is the surface gravitational acceleration.

## References

BIFROST Project (1996), GPS measurements to constrain geodynamic processes in Fennoscandia, *Eos Trans. AGU*, *77*, 337, 341.

Davis, J. L., J. X. Mitrovica, H.-G. Scherneck, and H. Fan (1999), Investigations of Fennoscandian glacial isostatic adjustment using model sea level records, *J. Geophys. Res.*, *104*, 2733–2747.

Dziewonski, A. M., and D. L. Anderson (1981), Preliminary Reference Earth Model (PREM), *Phys. Earth Planet. Inter.*, *25*, 297–356.

Farrell, W. E., and J. A. Clark (1976), On postglacial sea level, *Geophys. J. R. Astron. Soc.*, *46*, 647–667.

Fjeldskaar, W. (1994), Viscosity and thickness of the asthenosphere detected from the Fennoscandian uplift, *Earth Planet. Sci. Lett.*, *126*, 399–410.

Han, D., and J. Wahr (1989), Post-glacial rebound analysis for a rotating Earth, in *Slow Deformations and Transmission of Stress in the Earth*, *Geophys. Monogr. Ser.*, vol. 49, edited by S. Cohen and P. Vaníček, pp. 1–6, AGU, Washington, D. C.

Haskell, N. A. (1935), The motion of the fluid under a surface load, 1, *Physics*, *6*, 265–269.

James, T. S., and A. Lambert (1993), A comparison of VLBI data with the ICE-3G glacial rebound model, *Geophys. Res. Lett.*, *20*, 871–874.

Johansson, J. M., et al. (2002), Continuous GPS measurements of postglacial adjustment in Fennoscandia: 1. Geodetic results, *J. Geophys. Res.*, *107*(B8), 2157, doi:10.1029/2001JB000400.

Karato, S., and P. Wu (1993), Rheology of the upper mantle: A synthesis, *Science*, *260*, 771–778.

Kaufmann, G., and K. Lambeck (2002), Glacial isostatic adjustment and the radial viscosity profile from inverse modeling, *J. Geophys. Res.*, *107*(B11), 2280, doi:10.1029/2001JB000941.

Kaufmann, G., and P. Wu (2002), Glacial isostatic adjustment on a three-dimensional laterally heterogeneous earth: Examples from Fennoscandia and the Barents Sea, in *Ice Sheets, Sea Level and the Dynamic Earth*, *Geodyn. Ser.*, vol. 29, edited by J. X. Mitrovica and L. L. A. Vermeersen, pp. 293–309, AGU, Washington, D. C.

Lambeck, K., P. Johnston, and M. Nakada (1990), Holocene glacial rebound and sea-level change in NW Europe, *Geophys. J. Int.*, *103*, 451–468.

Lambeck, K., C. Smither, and P. Johnston (1998a), Sea-level change, glacial rebound and mantle viscosity for northern Europe, *Geophys. J. Int.*, *134*, 102–144.

Lambeck, K., C. Smither, and M. Ekman (1998b), Tests of glacial rebound models for Fennoscandinavia based on instrumented sea- and lake-level records, *Geophys. J. Int.*, *135*, 375–387.

Mäkinen, J., H. Koivula, M. Poutanen, and V. Saaranen (2003), Vertical velocities in Finland from permanent GPS networks and from repeated precise levelling, *J. Geodyn.*, *35*, 443–456.

McConnell, R. K. (1968), Viscosity of the mantle from relaxation time spectra of isostatic adjustment, *J. Geophys. Res.*, *73*, 7089–7105.

Milne, G. A. (1998), Refining models of the glacial isostatic adjustment process, Ph.D. thesis, Univ. of Toronto, Toronto, Ont., Canada.

Milne, G. A., J. X. Mitrovica, and J. L. Davis (1999), Near-field hydro-isostasy: The implementation of a revised sea-level equation, *Geophys. J. Int.*, *139*, 464–482.

Milne, G. A., J. L. Davis, J. X. Mitrovica, H.-G. Scherneck, J. M. Johansson, M. Vermeer, and H. Koivula (2001), Space-geodetic constraints on glacial isostatic adjustment in Fennoscandia, *Science*, *291*, 2381–2385.

Mitrovica, J. X. (1996), Haskell [1935] revisited, *J. Geophys. Res.*, *101*, 555–569.

Mitrovica, J. X., and A. M. Forte (1997), Radial profile of mantle viscosity: Results from the joint inversion of convection and postglacial rebound observables, *J. Geophys. Res.*, *102*, 2751–2769.

Mitrovica, J. X., and G. A. Milne (1998), Glaciation-induced perturbations in the Earth's rotation: A new appraisal, *J. Geophys. Res.*, *103*, 985–1005.

Mitrovica, J. X., and W. R. Peltier (1991), On postglacial geoid subsidence over the equatorial oceans, *J. Geophys. Res.*, *96*, 20,053–20,071.

Mitrovica, J. X., and W. R. Peltier (1993), A new formalism for inferring mantle viscosity based on estimates of postglacial decay times: Applica-

tion to RSL variations in N.E. Hudson Bay, *Geophys. Res. Lett.*, *20*, 2183–2186.

Mitrovica, J. X., J. L. Davis, and I. I. Shapiro (1993), Constraining proposed combinations of ice history and Earth rheology using VLBI determined baseline length rates in North America, *Geophys. Res. Lett.*, *20*, 2387–2390.

Mitrovica, J. X., J. L. Davis, and I. I. Shapiro (1994a), A spectral formalism for computing three dimensional deformations due to surface loads: 1. Theory, *J. Geophys. Res.*, *99*, 7057–7073.

Mitrovica, J. X., J. L. Davis, and I. I. Shapiro (1994b), A spectral formalism for computing three dimensional deformations due to surface loads: 2. Present-day glacial isostatic adjustment, *J. Geophys. Res.*, *99*, 7075–7101.

Mitrovica, J. X., G. A. Milne, and J. L. Davis (2001), Glacial isostatic adjustment on a rotating Earth, *J. Geophys. Int.*, *147*, 562–578.

Nakada, M., and K. Lambeck (1989), Late Pleistocene and Holocene sea-level change in the Australian region and mantle rheology, *Geophys. J. Int.*, *96*, 497–517.

Peltier, W. R. (1974), The impulse response of a Maxwell Earth, *Rev. Geophys.*, *12*, 649–669.

Peltier, W. R., and J. T. Andrews (1976), Glacial isostatic adjustment-I. The forward problem, *Geophys. J. R. Astron. Soc.*, *46*, 605–646.

Sabadini, R., and B. Vermeersen (1997), Ice-age cycles: Earth's rotation instabilities and sea-level changes, *Geophys. Res. Lett.*, *24*, 3041–3044.

Sabadini, R., D. A. Yuen, and E. Boschi (1982), Polar wander and the forced responses of a rotating, multilayered, viscoelastic planet, *J. Geophys. Res.*, *87*, 2885–2903.

Scherneck, H.-G., J. M. Johansson, H. Koivula, T. van Dam, and J. L. Davis (2003), Vertical crustal motion observed in the BIFROST project, *J. Geodyn.*, *35*, 425–441.

Tarantola, A., and B. Valette (1982), Generalized non-linear inverse problems solved using the least squares criterion, *Rev. Geophys.*, *20*, 219–232.

Tushingham, A. M., and W. R. Peltier (1991), ICE-3G: A new global model of late Pleistocene deglaciation based on geophysical predictions of postglacial relative sea level change, *J. Geophys. Res.*, *96*, 4497–4523.

Veining Meinesz, F. A. (1937), The determination of the Earth's plasticity from the post-glacial uplift of Scandinavia: Isostatic adjustment, *K. Akad. Wet.*, *40*, 654–662.

Wahr, J. M., and J. L. Davis (2002), Geodetic constraints on glacial isostatic adjustment, in *Ice Sheets, Sea Level and the Dynamic Earth*, *Geodyn. Ser.*, vol. 29, edited by J. X. Mitrovica and L. L. A. Vermeersen, pp. 3–32, AGU, Washington, D. C.

Wessel, P., and W. H. F. Smith (1991), Free software helps map and display data, *Eos Trans. AGU*, *72*, 441, 445–446.

Wieczerkowski, K., J. X. Mitrovica, and D. Wolf (1999), A revised relaxation spectrum for Fennoscandia, *Geophys. J. Int.*, *139*, 69–86.

Wolf, D. (1987), An upper bound on lithospheric thickness from glacio-isostatic adjustment in Fennoscandia, *J. Geophys.*, *61*, 141–149.

Wu, P. (1978), The response of a Maxwell earth to applied surface mass loads: Glacial isostatic adjustment, M.Sc. thesis, Univ. of Toronto, Toronto, Ont., Canada.

Wu, P. (1999), Modelling postglacial sea levels with power-law rheology and a realistic ice model in the absence of ambient tectonic stress, *Geophys. J. Int.*, *139*, 691–702.

Wu, P., and W. R. Peltier (1982), Viscous gravitational relaxation, *Geophys. J. R. Astron. Soc.*, *70*, 435–485.

Wu, P., and W. R. Peltier (1984), Pleistocene deglaciation and the Earth's rotation: A new analysis, *Geophys. J. R. Astron. Soc.*, *76*, 753–792.

————————

J. L. Davis, Harvard-Smithsonian Center for Astrophysics, 60 Garden Street, MS-42, Cambridge, MA 02138, USA. (jdavis@cfa.harvard.edu)
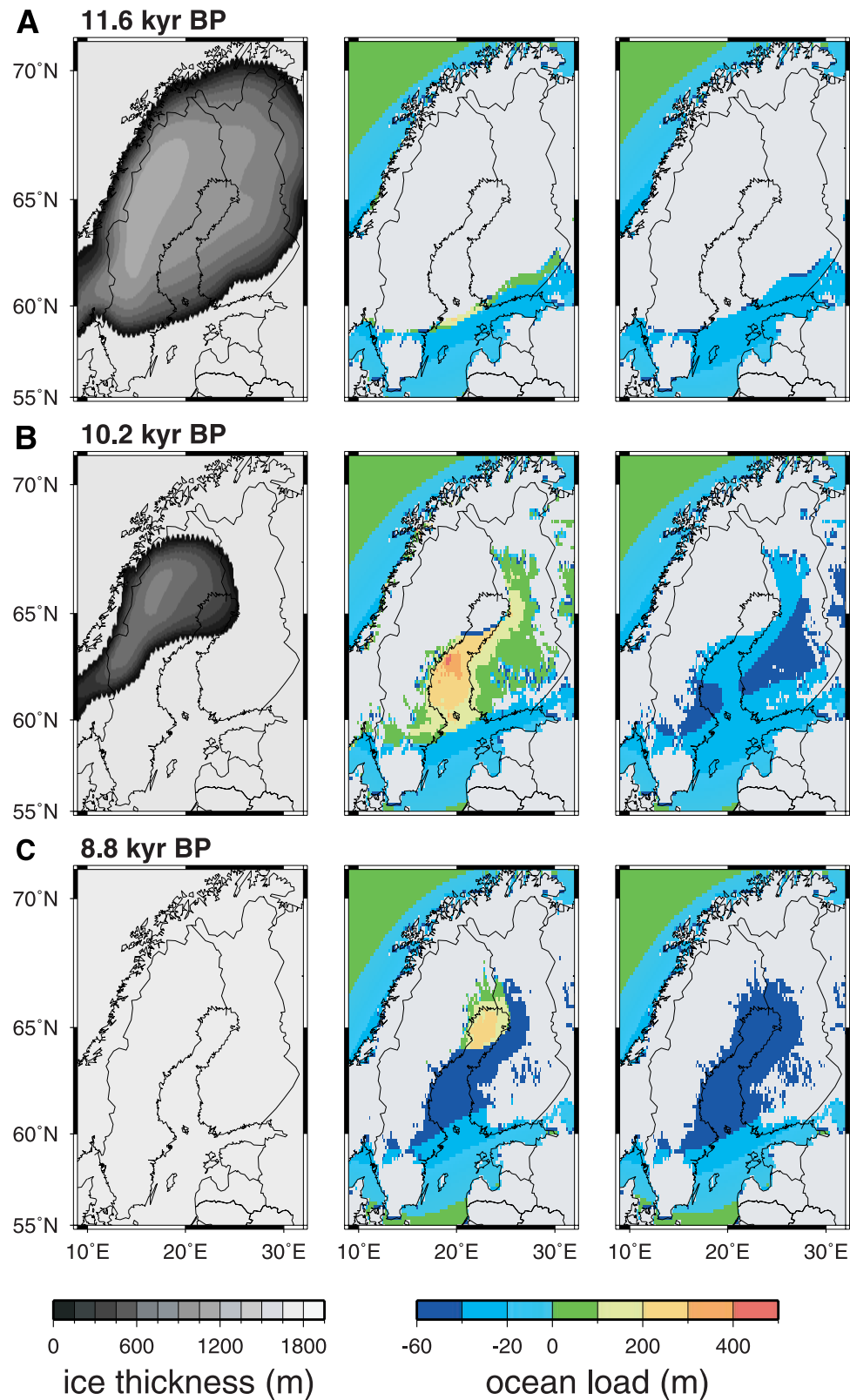
J. M. Johansson and H.-G. Scherneck, Onsala Space Observatory, Chalmers University of Technology, SE-439 92, Onsala, Sweden. (hgs@oso.chalmers.se)

H. Koivula, Finnish Geodetic Institute, Geodeetinrinne 2, Masala, FIN-02431, Finland. (hannu.koivula@fgi.fi)

G. A. Milne, Department of Earth Sciences, University of Durham, Science Labs, Durham, DH1 3LE, UK. (g.a.milne@durham.ac.uk)

J. X. Mitrovica, Department of Physics, University of Toronto, 60 St. George St., Toronto, Ontario, Canada M5S 1A7. (jxm@physics.utoronto.ca)

M. Vermeer, Institute of Geodesy and Cartography, Helsinki University of Technology, P.O. Box 1200, Hut, FIN-02015, Finland. (martin.vermeer@hut.fi)

**Figure 3.** Components of the regional surface load during the last stages of deglaciation. (left) Ice thickness at the times (a) 11.6, (b) 10.2, and (c) 8.8 ka. These times correspond to the calibrated $^{14}$C timescale. (middle and right) Predicted ocean load at the corresponding time steps predicted via the revised [*Milne et al.*, 1999] and original [*Farrell and Clark*, 1976] sea level equations, respectively. In Figure 3 (middle and right) the areas with light grey shading denote regions that are either ice covered or above contemporaneous sea level.